Paleoceanography and Paleoclimatology

RESEARCH ARTICLE
10.1029/2018PA003349

Early Pleistocene Obliquity-Scale pCO_2 Variability at ~1.5 Million Years Ago

Kelsey A. Dyez[1,2], Bärbel Hönisch[1,3], and Gavin A. Schmidt[4]

[1]Lamont-Doherty Earth Observatory, Columbia University, New York, NY, USA, [2]Now at Department of Earth and Environmental Sciences, University of Michigan, Ann Arbor, MI, USA, [3]Department of Earth and Environmental Sciences, Columbia University, New York, NY, USA, [4]NASA Goddard Institute for Space Studies, New York, NY, USA

Key Points:
- Early Pleistocene pCO_2 roughly varied with obliquity cycles
- Interglacial pCO_2 was similar in the early and late Pleistocene; glacial pCO_2 declined over the mid-Pleistocene transition
- Discrepancies between $\delta^{11}B$ values and corresponding pCO_2 estimates from *G. ruber* and *T. sacculifer* are observed and may indicate evolving vital effects

Supporting Information:
- Supporting Information S1
- Figure S1
- Figure S2
- Figure S3
- Figure S4

Correspondence to:
K. A. Dyez,
kdyez@umich.edu

Citation:
Dyez, K. A., Hönisch, B., & Schmidt, G. A. (2018). Early Pleistocene obliquity-scale pCO_2 variability at ~1.5 million years ago. *Paleoceanography and Paleoclimatology*, *33*, 1270–1291. https://doi.org/10.1029/2018PA003349

Received 5 MAR 2018
Accepted 31 OCT 2018
Accepted article online 5 NOV 2018
Published online 23 NOV 2018

Abstract In the early Pleistocene, global temperature cycles predominantly varied with ~41-kyr (obliquity-scale) periodicity. Atmospheric greenhouse gas concentrations likely played a role in these climate cycles; marine sediments provide an indirect geochemical means to estimate early Pleistocene CO_2. Here we present a boron isotope-based record of continuous high-resolution surface ocean pH and inferred atmospheric CO_2 changes. Our results show that, within a window of time in the early Pleistocene (1.38–1.54 Ma), pCO_2 varied with obliquity, confirming that, analogous to late Pleistocene conditions, the carbon cycle and climate covaried at ~1.5 Ma. Pairing the reconstructed early Pleistocene pCO_2 amplitude (92 ± 13 μatm) with a comparably smaller global surface temperature glacial/interglacial amplitude (3.0 ± 0.5 K) yields a surface temperature change to CO_2 radiative forcing ratio of $S_{[CO2]}$~0.75 (±0.5) $°C^{-1}{\cdot}W^{-1}{\cdot}m^{-2}$, as compared to the late Pleistocene $S_{[CO2]}$ value of ~1.75 (±0.6) $°C^{-1}{\cdot}W^{-1}{\cdot}m^{-2}$. This direct comparison of pCO_2 and temperature implicitly incorporates the large ice sheet forcing as an internal feedback and is not directly applicable to future warming. We evaluate this result with a simple climate model and show that the presumably thinner, though extensive, northern hemisphere ice sheets would increase surface temperature sensitivity to radiative forcing. Thus, the mechanism to dampen actual temperature variability in the early Pleistocene more likely lies with Southern Ocean circulation dynamics or antiphase hemispheric forcing. We also compile this new carbon dioxide record with published Plio-Pleistocene $\delta^{11}B$ records using consistent boundary conditions and explore potential reasons for the discrepancy between Pliocene pCO_2 based on different planktic foraminifera.

1. Introduction

The Pleistocene Epoch was characterized by a sequence of glacial/interglacial climate oscillations that are recorded in geochemical records from deep-sea sediments, continental deposits, and ice cores (e.g., Imbrie et al., 1984; Joannin et al., 2010; Lüthi et al., 2008). These records show that Earth's surface temperature covaried with the dominant periodicities of Earth's orbit around the Sun: orbital precession, obliquity, and/or eccentricity. Nevertheless, understanding how the climate system responds to and amplifies the initial orbital insolation forcing is a long-standing problem in the field of paleoclimatology (Hansen et al., 1984, 2005; Hays et al., 1976; Imbrie et al., 1992). High-resolution records of temperature and greenhouse gas concentrations are of paramount value to elucidate the pattern and drivers of global climate change, yet continuous high-resolution ice core records of trapped ancient air are thus far restricted to the late Pleistocene (0.8 Ma to present; e.g., Lüthi et al., 2008). Ancient air inclusions in late Pleistocene ice-cores suggest that the partial pressure of atmospheric CO_2 (pCO_2) lagged an initial temperature perturbation (Fischer et al., 2010) such that radiative greenhouse gas forcing at most amplified the orbital pacing of Pleistocene climate, via carbon cycle feedbacks, deep-sea carbon storage and release, and radiative forcing (Anderson et al., 2009; Shakun et al., 2012). During the early Pleistocene (2.6–1.0 Ma), obliquity set the dominant tempo of climate, and cold glacial intervals were shorter and less extreme (e.g., Huybers, 2007; Lisiecki & Raymo, 2005). The presence of North American glacial tills indicates that early Pleistocene ice sheets at glacial maxima extended as far south as 39°N (Balco & Rovey, 2010; Roy et al., 2004).

In the early Pleistocene, both tropical (e.g., Herbert et al., 2010) and extratropical (e.g., Lawrence et al., 2009; Martínez-Garcia et al., 2010) sea surface temperature (SST) records reveal long-term cooling in both glacial and interglacial intervals (i.e., 2 K cooler in tropics and 3–4 K cooler in high latitudes). At the same time, the glacial-interglacial amplitude of surface temperature increased from ~3 to ~5 K from the early to late

Pleistocene, as glacial temperatures cooled (Herbert et al., 2010; Lawrence et al., 2009; Martínez-Garcia et al., 2010). The gradual cooling of the early Pleistocene glacials culminated in the mid-Pleistocene transition (MPT) when surface temperature and benthic $\delta^{18}O$ records shifted from a dominant 41-kyr periodicity to ~100-kyr pacing, albeit without an obvious corresponding change in the periodicity of incoming solar radiation (Clark et al., 2006; Ruddiman et al., 1989). Mechanisms put forward to explain this shift in climate response at the MPT include the exposure of crystalline bedrock and thus a more solid foundation for the Laurentide ice sheet (e.g., Clark & Pollard, 1998), changing ocean dynamics that provide increased precipitation available to build larger northern hemisphere ice sheets (McClymont et al., 2008; Tziperman & Gildor, 2003), or the consequence of long-term cooling and glacial CO_2 drawdown as a result of iron fertilization and/or reduced ocean ventilation which sequestered more carbon in the deep ocean (Chalk et al., 2017; Hönisch et al., 2009; Köhler & Bintanja, 2008). Filling in the early Pleistocene pCO_2 data gaps with orbitally resolved records will help to evaluate these hypotheses.

While efforts to extend the continuous ice-core pCO_2 record to the early Pleistocene are being actively pursued (Bibby et al., 2016; Fischer et al., 2013; Higgins et al., 2015; Witze, 2015), such records are not yet available. However, marine sediments provide an opportunity to estimate pCO_2 changes from earlier and warmer periods of Earth history. One leading method for estimating atmospheric pCO_2 from marine sediments is via the boron isotope ratio ($\delta^{11}B$) recorded in the shells of planktic foraminifera. Shell $\delta^{11}B$ is primarily controlled by seawater acidity (i.e., pH). CO_2 exchanges between the atmosphere and the surface ocean depend on the partial pressure in each medium after Henry's law. Higher atmospheric pCO_2 results in more CO_2 dissolved in seawater and thereby lowers surface ocean pH. The pH dependency of the relative abundance and isotopic signature of the two main species of boron in seawater (borate ion and boric acid) permits the $\delta^{11}B$ value of marine carbonates to reflect such changes in ocean pH (see section 2). Several studies have validated this proxy relative to ice core pCO_2 in the late Pleistocene (Chalk et al., 2017; Henehan et al., 2013; Hönisch & Hemming, 2005) and presented estimates of pCO_2 throughout portions of the Pliocene and Pleistocene (Bartoli et al., 2011; Chalk et al., 2017; Henehan et al., 2013; Hönisch et al., 2009; Martínez-Botí, Foster et al., 2015). Here we present estimates of pCO_2 based on new $\delta^{11}B$ measurements in planktic foraminifera shells within a time window spanning Marine Isotope Stages (MISs) 44–52 (1.38–1.54 Ma).

Published estimates of early Pleistocene pCO_2 are as high as 410 (±50) μatm as recorded at Ocean Drilling Program (ODP) Site 999 at 2.37 Ma (Martínez-Botí, Foster et al., 2015) and as low as 167 (±19) μatm at 0.65 Ma (Hönisch et al., 2009). Bartoli et al. (2011) observed that atmospheric pCO_2 decreased in a stepwise fashion at ~2.7 Ma, although that particular study did not measure a temperature proxy alongside each of the boron isotope analyses, and used modeled estimates of the carbonate ion concentration, $[CO_3^{2-}]$, as the second parameter of the carbonate system to translate pH into reconstructed pCO_2. Here we present new high-resolution data from ODP 668B in the eastern tropical Atlantic, revise the data set of Bartoli et al. (2011) with new temperature and geochemical constraints, and compile these records in a consistent manner with other published data sets of early Pleistocene pCO_2. By minimizing the differences in the way boundary conditions are treated among these records, we are able to compare the combined $\delta^{11}B$ and pCO_2 records and to describe coherent features of the pCO_2 decline from the late Pliocene through the Pleistocene.

2. Materials and Methods

The primary materials for this study come from ODP Site 668B in the eastern tropical Atlantic (4.77°N, 20.93°W, water depth 2,693 m, average sedimentation rate 1.5 cm/kyr, Figure 1). The modern surface ocean at this location is near equilibrium with the atmosphere with respect to CO_2 (Takahashi et al., 2009), and previously published late Pleistocene boron isotope data from this site show good agreement with ice core pCO_2 over the past 0.8 Ma (Hönisch et al., 2009; Hönisch & Hemming, 2005), making this a promising location for extending the reconstruction of paleo-pCO_2. Sediment samples were taken from core 668B every 5 cm (3.3 kyr) and were selected to include glacial and interglacial extrema in planktic $\delta^{18}O$ (Hönisch et al., 2009). Samples were washed and picked for the planktic foraminiferal species *Globigerinoides ruber* (300–355 μm size fraction) and *Trilobatus* (formerly *Globigerinoides*) *sacculifer* (>500 μm size fraction), which both live in the surface-mixed layer (Spero et al., 2003).

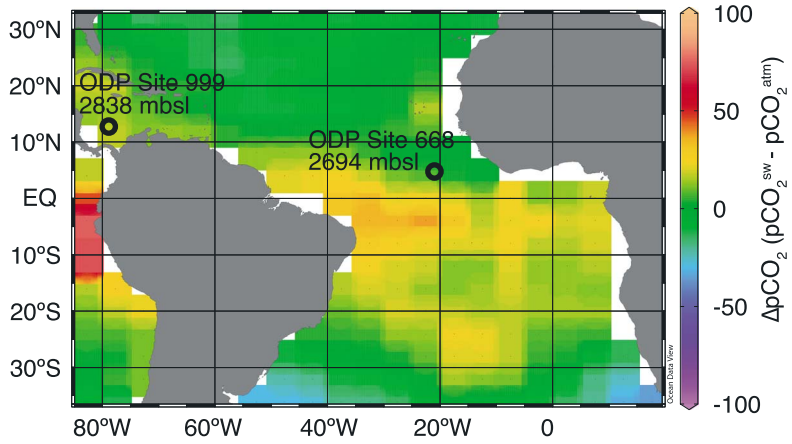

Figure 1. New geochemical data presented are from eastern equatorial Atlantic site ODP 668B and from Caribbean site ODP 999A. Background colors are modern mean annual ΔpCO_2 (seawater pCO_2 − atmosphere pCO_2; Takahashi et al., 2009) and are plotted using Ocean Data View 4 (Schlitzer, 2017). Today surface water pCO_2 in these locations is near equilibrium with the atmosphere. ODP = Ocean Drilling Program.

2.1. δ^{11}B-Based pCO_2 Estimates

Tests of *T. sacculifer* from the >500 μm size fraction have been validated to reflect surface ocean conditions for pH and pCO_2 estimates (Hönisch et al., 2009; Hönisch & Hemming, 2004, 2005). Although partial dissolution has the potential to lower foraminiferal δ^{11}B in corrosive bottom water, this effect is more pronounced in smaller foraminiferal test size classes (Edgar et al., 2015; Hönisch & Hemming, 2004). The samples in this study come from the largest size fraction and from relatively shallow (2,693 modern m depth) waters that are oversaturated with respect to calcite ($\Omega_{calcite}$ = 1.5, Δ [CO_3^{2-}] ~35 μmol/kg). This depth is well above the regional lysocline and partial dissolution is unlikely (Regenberg et al., 2006). For each δ^{11}B sample, ~30–50 *T. sacculifer* shells were picked, gently crushed, and cleaned by repeated sonication in MilliQ water and methanol, oxidation in a buffered H_2O_2 solution to remove organic material, and a final weak acid leach (Barker et al., 2003). Cleaned material was rinsed in MilliQ water, dried to determine the calcite mass after cleaning, and finally dissolved in 2 N hydrochloric acid just before analysis. All δ^{11}B samples were measured at the Lamont-Doherty Earth Observatory using a TRITON thermal ionization mass spectrometer in negative mode (N-TIMS). Aliquots of the sample solution containing ≥1 ng boron were loaded onto outgassed zone-refined rhenium filaments, along with 1 μl of boron-free seawater to enhance ionization (see Hönisch et al., 2009, for details). Although analysis of boron isotopes in marine carbonates by the N-TIMS method yields ~1‰ higher δ^{11}B values compared to the alternative Multicollector Inductively Coupled Plasma Mass Spectrometer (MC-ICP-MS) technique, the relative variability between different samples is similar between the two methods and yield equivalent pH and pCO_2 results when technique-specific $\delta^{11}B_{foraminifera}$ versus $\delta^{11}B_{borate}$ calibrations are applied (J. R. Farmer et al., 2016; Foster et al., 2013). To minimize analytical uncertainty, each sample analysis was replicated 3–10 (average of 7) times. Of those replicates, individual analyses were rejected if excessive fractionation ($\delta^{11}B > 1‰$) occurred over the 40 min of data acquisition; 14% of analyses were rejected on this basis. The majority of samples yielded five or more replicates that met the acceptance criteria. Only one sample, at 1.436 Ma, could not be replicated due to low abundance of *T. sacculifer* shells. Uncertainty in the δ^{11}B measurement was determined as the larger of either (1) the standard error in valid replicate analyses (i.e., 2σ = 2 * standard deviation / √N, where N is the number of accepted replicates) or (2) the 2σ uncertainty of an equal number of repeat measurements of an in-house standard of NIST 951 precipitated in $CaCO_3$ matrix (vaterite). Average 2σ uncertainty of all δ^{11}B measurements is ±0.26‰.

The relative abundance of the two aqueous species of boron in seawater, borate ion ($B(OH)_4^-$) and boric acid ($B(OH)_3$), is pH dependent (Dickson, 1990; Hemming & Hanson, 1992). The isotopic fractionation between ^{11}B (natural abundance ~80%) and ^{10}B (~20%) generates a constant δ^{11}B offset between these two aqueous boron species, such that δ^{11}B of borate increases with the relative abundance of borate at higher pH. Since the borate ion is the primary species incorporated into foraminiferal calcite (e.g., Branson et al., 2015; Hemming & Hanson, 1992), in situ seawater pH can be estimated from the δ^{11}B of foraminiferal calcite.

The boron isotopic composition of seawater ($\delta^{11}B_{sw}$) must also be known; in the modern ocean $\delta^{11}B_{sw}$ is 39.61 (±0.04)‰ (Foster et al., 2010). While this value likely increased over the Cenozoic through shifts in weathering and/or volcanic emissions (Lemarchand et al., 2000), attempts to reconstruct $\delta^{11}B_{sw}$ over the past 5 million years have yielded disparate results. The combined evidence, whether from benthic foraminiferal $\delta^{11}B$ alongside modeled ocean pH (Raitzsch & Hönisch, 2013) or paired $\delta^{11}B$ measurements in the water column coupled with assumptions about water column pH gradient (Greenop et al., 2017; Pearson & Palmer, 2000), shows no clear indication of a trend in $\delta^{11}B_{sw}$ over the past 5 Ma (Figure S1). As the residence time of boron in seawater is long (11–17 Ma), the maximum rate of change over this time period is likely <0.1‰ per million years (Lemarchand et al., 2000); hence, we apply the modern $\delta^{11}B_{sw}$ value (39.61‰) to all Plio-Pleistocene samples and increase the uncertainty of this assumed value at a constant rate of 0.1‰ per million years (Figure S1). Ocean pH is then determined via:

$$\mathrm{pH} = \mathrm{p}K^{*}_{B} - \log\left[-\left(\delta^{11}B_{sw} - \delta^{11}B_{borate}\right)/\left\{\delta^{11}B_{sw} - \left({}^{11\text{-}10}K_{B}{}^{*}\,\delta^{11}B_{borate}\right) - 1000^{*}\left({}^{11\text{-}10}K_{B} - 1\right)\right\}\right], \quad (1)$$

where pK^{*}_{B} is the dissociation constant for boric acid at in situ temperature, salinity, and pressure (Dickson, 1990; Millero, 1995), and the aqueous boron isotope fractionation factor is ${}^{11\text{-}10}K_{B}$ = 1.0272 (±0.0006) (Klochko et al., 2006). Application of the boron isotope proxy also requires an understanding of any physiological or vital effects on the pH of the foraminiferal microenvironment, which have been documented for a variety of species. Here we use a calibration specifically established for *T. sacculifer*, which includes culture and core top sediment samples of *T. sacculifer* measured via N-TIMS at LDEO and Stony Brook (Hönisch et al., 2009; Hönisch & Hemming, 2004, 2005; Sanyal et al., 2001). Values measured at Stony Brook have been cross-calibrated with N-TIMS (Hönisch et al., 2009) and a constant offset of −1.1‰ has been applied to all data measured in Stony Brook to shift them onto data measured on the N-TIMS at LDEO. A linear York fit (York et al., 2004) calculated for laboratory cultured specimens grown across a range of pH values includes uncertainties in the $\delta^{11}B_{calcite}$ measurement and the $\delta^{11}B_{borate}$ calculation for experimental seawater. This regression is then adjusted by a constant intercept offset of −0.84‰ so as to pass through the average of core top *T. sacculifer* $\delta^{11}B_{calcite}$ data and the corresponding preindustrial $\delta^{11}B_{borate}$ (Figure 2 and Table S1). The offset accounts for the difference between cultured and sedimentary specimens, which is likely due to the gametogenic calcite crust that *T. sacculifer* secretes at greater water depths in the ocean (Bé, 1980). The resulting calibration for *T. sacculifer* in the >500 μm size fraction (measured on N-TIMS), including 2σ uncertainty, is

$$\delta^{11}B_{borate} = \left[\delta^{11}B_{T.sacculifer\ N-TIMS} - 6.42\ (\pm 1.64)\right]/0.73\ (\pm 0.08). \quad (2)$$

In comparison, the published calibration for *T. sacculifer* using the MC-ICP-MS technique (Martínez-Botí, Marino et al., 2015) is

$$\delta^{11}B_{borate} = \left[\delta^{11}B_{T.sacculifer\ MC-ICP-MS} - 3.60\ (\pm 0.72)\right]/0.83\ (\pm 0.04). \quad (3)$$

While the slope of the MC-ICP-MS $\delta^{11}B_{borate}$ calibration is steeper (0.83 vs 0.73), the additional culture data points in our N-TIMS calibration (5 instead of 3) allow for a more precise calibration. The primary difference between these technique-specific calibrations is the intercept value, which is the most important factor in aligning pH estimates from N-TIMS and MC-ICP-MS $\delta^{11}B$ analyses (Foster et al., 2013).

2.2. Temperature, Salinity, and Pressure Estimates

Here we present new Mg/Ca-based estimates of SST using *G. ruber* from Site 668B and *T. sacculifer* from Site 999A. Due to the limited availability of large *T. sacculifer* tests from Site 668B, tests of *G. ruber* (sensu stricto, white) were used to estimate surface ocean temperature for this site. *G. ruber* shares the near-surface ocean habitat of large *T. sacculifer* specimens (E. C. Farmer et al., 2007; Ravelo & Fairbanks, 1992; Spero et al., 2003). For Site 668B, 40–60 *G. ruber* tests were picked from the 300–355 μm size fraction. For Site 999A, 40 shells of *T. sacculifer* were picked from the 425–500 μm size fraction, the same species and size fraction of planktic foraminifera as the original $\delta^{11}B$ data (Bartoli et al., 2011). Shells were then gently broken and cleaned following established protocol including both the oxidative and reductive steps (Boyle & Keigwin, 1985; Mashiotta et al., 1999). Inclusion of the reductive step is generally preferred for Mg/Ca analysis as it is more effective at removing high-Mg contaminants such as authigenic metals precipitated after deposition in the sediment, even

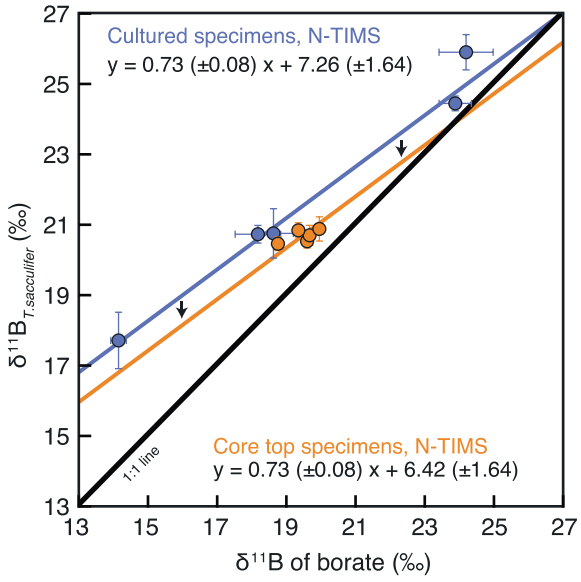

Figure 2. Calibration of $\delta^{11}B$ of *T. sacculifer* as measured by N-TIMS versus $\delta^{11}B$ of borate in seawater (data in Table S1). Culture data (Sanyal et al., 2001, and this study) define the slope of the relationship. Core top $\delta^{11}B$ data are offset from the culture relationship, where the offset can be explained by secretion of gametogenic calcite at greater water depth. This offset (0.84‰) is subtracted from the intercept of the culture regression to define the sedimentary calibration of $\delta^{11}B_{T.\ sacculifer}$ calcite to $\delta^{11}B$ borate. Linear regression is a York fit (York et al., 2004, Matlab script York_fit.m) which incorporates *x* and *y* uncertainty for each datum; slope and intercept uncertainties are 2σ. N-TIMS = thermal ionization mass spectrometer in negative mode.

though it has been shown to lower Mg/Ca values beyond their original value (Martin & Lea, 2002; Weldeab et al., 2006). Because the Mg/Ca-temperature calibration we use (Anand et al., 2003) is based on sediment trap samples and therefore did not apply reductive cleaning, we account for reductive cleaning bias by adding 10% to the measured Mg/Ca ratio of our samples (Martin & Lea, 2002). Mg/Ca ratios were measured via ICP-MS (iCAP-Q) at the Lamont-Doherty Earth Observatory. The 2σ standard error for repeated measurements of internal foraminifer reference standards is ±2.2%, or ~ ± 0.08 mmol/mol. This SST calibration carries a larger uncertainty (±2.4 K, 2σ) than that of the Mg/Ca measurement uncertainty (~ ± 0.24 K) and we adopt the larger calibration uncertainty for seawater temperature estimates. As our samples are derived from a time period when the Mg/Ca value of seawater (Mg/Ca_{sw}) was likely lower than the modern value of 5.2 mmol/mol, a correction is needed for this change in seawater constituents (Delaney et al., 1985; Evans et al., 2016; Fantle & DePaolo, 2005, 2006; Medina-Elizalde et al., 2008; O'Brien et al., 2014). To facilitate this correction, Mg/Ca_{sw} values are taken from reported pore fluid chemistry and numerical modeling (Figure S7, Fantle & DePaolo, 2006). This Mg/Ca_{sw} data set is within the uncertainty of Mg/Ca_{sw} values estimated from fluid inclusions in marine evaporites, the most recent of which is Messinian in age (5–6 Ma, Mg/Ca_{sw} ~3.6 mmol/mol; Brennan et al., 2013; Horita et al., 2002). If data from marine evaporite fluid inclusions were considered alone, and Mg/Ca_{sw} values are linearly extrapolated from 5.5 Ma to present, the resulting SST would be ~0.7 K lower and calculated pCO_2 would be ~5 μatm higher. The SST calibration we use includes the power law modification suggested by Evans and Müller (2012) and the *T. sacculifer* exponential H-value of 0.41 (Delaney et al., 1985; Evans & Müller, 2012):

$$SST\ (^{\circ}C) = \ln\left[\left((Mg/Ca)_{calcite}{}^{*}\left((Mg/Ca)_{sw}{}^{t=0}\right)^{H}\right)/\left(0.38^{*}\left((Mg/Ca)_{sw}{}^{t}\right)^{H}\right)\right]/0.09, \quad (4)$$

where $(Mg/Ca)^{t}_{sw}$ is the Mg/Ca ratio of seawater at time *t*. This approach is commonly used to reconstruct temperature in this time period (e.g., Chalk et al., 2017; Martínez-Botí, Foster et al., 2015). The correction for dissolution with depth (Dekens et al., 2002) is omitted for all records in this study, as all study sites are well above the regional tropical Atlantic lysocline (4,200 m water depth), and bottom water is saturated with respect to calcium carbonate (Key et al., 2004; Regenberg et al., 2006). Hönisch et al. (2013) have demonstrated that adjusting Mg/Ca data from sediments above the lysocline effectively overestimates actual calcification temperatures.

Pleistocene salinity was calculated as a function of relative mean sea level (RMSL) as determined via a numerical ice-ocean model (Bintanja & van de Wal, 2008). The change in local salinity is approximately proportional to the change in global average salinity due to glacial-interglacial sea level change. The equation used is

$$Salinity_{668B} = 35.8‰ + RMSL/3,800\ m^{*}\ 34.8‰, \quad (5)$$

where 35.8‰ is the modern salinity of the mixed layer (50 m water depth) at Site 668B (Zweng et al., 2013), 3,800 m is the average depth of the ocean, and 34.8‰ is the average salinity of the modern ocean. These estimates agree (within uncertainty) with local salinity estimates derived from using Mg/Ca-based SST and calcite $\delta^{18}O$ to estimate the $\delta^{18}O$ of seawater ($\delta^{18}O_{sw}$, Figure 3; Bemis et al., 1998; Legrande & Schmidt, 2006).

In situ seawater pressure is also required and is a function of the foraminiferal calcification depth. Here we assume a calcification depth for both *G. ruber* and *T. sacculifer* of 50 m (E. C. Farmer et al., 2007; Schiebel & Hemleben, 2005) and a corresponding seawater pressure of 50 dbar. The pressure effect on equilibrium constants is small; an uncertainty of ±50 m water depth results in an uncertainty in calculated pH of ±0.002 and pCO_2 of ±1 μatm.

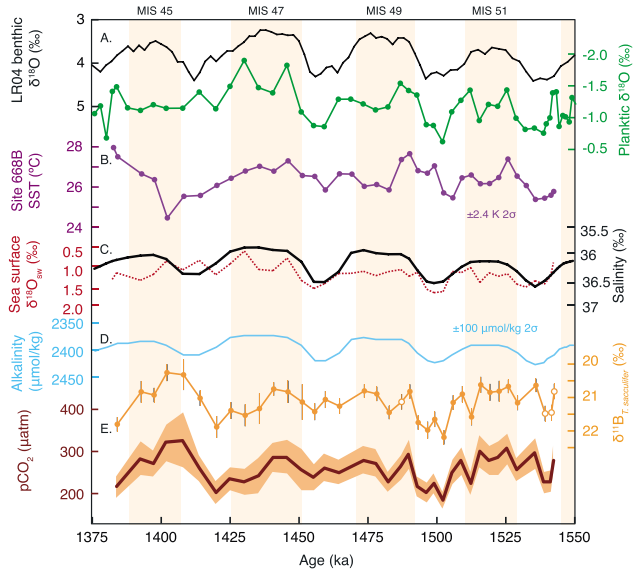

Figure 3. Site 668B orbital-scale records of the early Pleistocene from planktic foraminifera. (a) Site 668B planktic $\delta^{18}O$ data (green, Hönisch et al., 2009) reflect local temperature and $\delta^{18}O_{sw}$. (b) SST based on planktic Mg/Ca (purple, uncertainty is ±2.4 K (2σ)). (c) Calculated $\delta^{18}O_{sw}$ from planktic $\delta^{18}O$ and Mg/Ca-based SST (red) and compared with salinity modeled from global sea level (black, Bintanja & van de Wal, 2008). (d) Alkalinity based on local modern relationship with salinity. (e) Planktic $\delta^{11}B$ data contain minima and maxima in line with glacial and interglacial periods; uncertainty is 2σ and open circles are from Hönisch et al. (2009). Surface ocean pCO_2 is calculated using pH (as estimated from $\delta^{11}B$, SST, and salinity) and estimated alkalinity; the uncertainty band reflects the propagated 2σ uncertainty, the largest source of which is contributed by the analytical uncertainty of $\delta^{11}B_{calcite}$. SST = sea surface temperature; MIS = Marine Isotope Stage.

2.3. Alkalinity Estimates

In order to calculate the partial pressure of CO_2 in seawater, a second variable of the ocean carbonate system is required (e.g., Zeebe & Wolf-Gladrow, 2001). Here alkalinity is estimated from the modern local alkalinity-to-salinity relationship following the *constant alkalinity* scenario of previous studies, which assumes that total alkalinity in the ocean remained constant in the past (Hönisch et al., 2009; Hönisch & Hemming, 2005). The local alkalinity-to-salinity relationship was developed using WOCE and GLODAP databases (Key et al., 2004; Schlitzer, 2000) covering the area 0–10°N and 10–20°W (Hönisch et al., 2009; Hönisch & Hemming, 2005).

$$Total\ Alkalinity_{668B} = 65.62^{*}\ Salinity_{668B} + 22.84. \quad (6)$$

Over long timescales (tens to hundreds of thousands of years) the local alkalinity-to-salinity relationship could deviate from the modern relationship as a function of the Canadian Shield silicate weathering contribution to global weathering rates, where increased weathering would have added alkalinity to the ocean (Clark et al., 2006). Even though the relative contribution of such differential weathering is weakly constrained, the absolute impact on paleo-alkalinity is relatively small. Models show that varying the contribution of Canadian Shield weathering to the total ocean alkalinity budget of between 0% and 8% (Figure S2) only change the total ocean alkalinity in the Pleistocene by ~50 µmol/kg (Clark et al., 2006). To account for the potential effect of differential weathering on the local alkalinity-to-salinity ratio for past time periods, we include an alkalinity uncertainty of ±100 µmol/kg for the past 1.8 Ma.

2.4. Calculation of pCO_2

Aqueous CO_2 (differentiated as PCO_2) values are calculated from estimates of pH (total scale), alkalinity, salinity, temperature, and pressure using CO2SYS (version 2.3, Pierrot et al., 2006). Within this program, we selected the recommended default values of pK_1 and pK_2 from Lueker et al. (2000), $KHSO_4$ from Dickson (1990), KHF from Perez and Fraga (1987), and $[B]_T$ from Lee et al. (2010). As described above, aqueous PCO_2 at site 668B is in equilibrium with the atmosphere in the modern ocean (Takahashi et al., 2009) and comparison of boron isotope estimates with ice core records suggests it was also in equilibrium over the past 800 kyr (Hönisch et al., 2009; Hönisch & Hemming, 2005). We therefore interpret our aqueous paleo-PCO_2 estimates from Site 668B as equivalent to atmospheric paleo-pCO_2. In order to directly compare with $\delta^{11}B$ records from Site 999A, we translate $\delta^{11}B$-based aqueous PCO_2 records from Site 999 to atmospheric pCO_2 by subtracting the annual average preindustrial disequilibrium value (21 µatm) as justified by Henehan et al. (2013) who accounted for the modern seasonal ΔpCO_2 difference and a small correction for preindustrial PCO_2 (Gloor et al., 2003; Takahashi et al., 2009).

2.5. Uncertainty

Uncertainty in the pH estimate is a function of the propagated 2σ uncertainties in the $\delta^{11}B$ measurement on $\delta^{11}B_{borate}$, the uncertainty in $\delta^{11}B_{sw}$, and the effect of temperature and salinity uncertainties on the dissociation constants of boric and carbonic acid in seawater. We report uncertainty in pH as the root-mean-square error of the effect each parameter uncertainty has on pH: the $\delta^{11}B$ measurement and $\delta^{11}B_{borate}$ calibration (±0.03 pH units, ~80% coming from analytical uncertainty), the estimate of $\delta^{11}B_{sw}$ (±0.01 pH units at 1.5 Ma), the temperature constraints (calibration uncertainty equates to ±0.02 pH units), and salinity (±0.01 pH units). Uncertainty is calculated on a sample-by-sample basis; average total pH uncertainty of the Site 668B data is ±0.043 (2σ). Uncertainty in the pCO_2 calculation is likewise a function of uncertainty in the overall input parameters: the $\delta^{11}B$ measurement and calibration (±23 µatm), alkalinity (±12 µatm), and the effects of temperature (±19 µatm) and salinity (±3 µatm). Uncertainty in PCO_2 is similarly calculated on a sample-by-

sample basis; average total PCO_2 uncertainty is ±33 μatm (2σ) for the newly estimated PCO_2 values at ~1.5 Ma.

2.6. Chronology

The age model for ODP Site 668B was initially constructed from microfossil occurrence data and estimates of the depths of geomagnetic reversals (Shipboard Scientific Party, 1988). This initial chronology was later tuned through the alignment of glacial-interglacial cycles in the high-resolution planktic (*G. ruber*) $\delta^{18}O$ values of Site 668B (Bird & Cali, 1998, 2002; Hönisch et al., 2009) with the well-dated planktic $\delta^{18}O$ values of ODP Site 677 (Shackleton et al., 1990) and the LR04 benthic $\delta^{18}O$ stack (Lisiecki & Raymo, 2005). In order to resolve planktic $\delta^{18}O$ mismatches between Sites 668B and 677 during MIS 48–52 (1.45–1.53 ka), we used AnalySeries software (Paillard et al., 1996) to add tie points which refine the planktic $\delta^{18}O$ alignment. All ages younger than 1.3 Ma (19 m core depth) are unchanged from the previously published age model (Hönisch et al., 2009). The revised age model for the period prior to 1.3 Ma (core depths 19–26 m) improves the planktic $\delta^{18}O$ correlation coefficient (Pearson R^2) between Sites 677 and 668B from ~0.31 to ~0.40 and reconstructed ages are up to 15% younger than previously estimated (Figure S3). The updated age model also conforms to the original ODP geomagnetic constraints, which placed the top of the Olduvai reversal (1.78 Ma) at 2.725 m core depth (Shipboard Scientific Party, 1988), just beyond the oldest available $\delta^{18}O$ values from Site 668B (Figure S3). Unfortunately, the age uncertainty of the underlying benthic $\delta^{18}O$ stack is ±6 kyr in the early Pleistocene (Lisiecki & Raymo, 2005); this age uncertainty prevents the determination of leads or lags that are shorter than this confidence interval.

2.7. Comparison With Other $\delta^{11}B$-Based PCO_2 Records

For comparison between this new record and other previously published Pleistocene $\delta^{11}B$-based PCO_2 records, we compile PCO_2 estimates from $\delta^{11}B$ data from Site 668B and Site 999A in the tropical Atlantic. These two sites present a good comparison as ocean-atmosphere disequilibrium is small at both locations. In order to rule out methodological differences, we calculated PCO_2 from each published record using equivalent input parameters and technique-specific calibrations. The original Site 668B $\delta^{11}B_{T.\ sacculifer}$ data (Hönisch et al., 2009) are used to recalculate pH and PCO_2 using the above methods (section 2.1–2.6). The $\delta^{11}B$ calibration for this data set is updated (equation (2)) and $\delta^{11}B_{sw}$ is assumed to be 39.61‰ throughout. Temperature is calculated via the same Anand et al. (2003) calibration, after correcting for changes in seawater Mg/Ca (equation (4)).

The $\delta^{11}B_{T.\ sacculifer}$ data of ODP 999A (Bartoli et al., 2011) were also revised using similar methods described above. To do so, we first generated new Mg/Ca data from the same or adjacent samples used for $\delta^{11}B$ analysis (see section 2.2). In the original study, SST was interpolated from *T. sacculifer* Mg/Ca values (Groeneveld, 2005) with a different temporal resolution than the $\delta^{11}B$ samples; our new temperature data reduce the interpolation of temperature estimates. Furthermore, the original SST record used the depth-based dissolution correction of Dekens et al. (2002), along with an outdated modern Mg/Ca_{sw} value of 4.96 mmol/mol. Due to omission of the depth correction, the SST estimated for this record is on average 1.8 K cooler than SST in the original publication (Figure S4) which places interglacial SST in agreement with modern SST at this location, whether taken from an annual average of modern direct measurements (27.7 °C; Locarnini et al., 2013) or estimated from core top Mg/Ca values (28.2 °C; Henehan et al., 2013). Site 999A (water depth 2,839 m) is situated well above the regional lysocline (4,200 m) and *T. sacculifer* shells are not subject to preferential high-Mg calcite dissolution at this water depth (Regenberg et al., 2006). Taken together, the omission of the depth correction thus appears well justified.

Additionally, Bartoli et al. (2011) used modeled surface ocean $[CO_3^{2-}]$ estimates as the second parameter of the carbonate system and paired them with their $\delta^{11}B$-pH estimates and to calculate PCO_2. Because pH and $[CO_3^{2-}]$ are closely related in carbonate equilibria, pairing them in carbon system calculations produces large variations in the calculated parameters. For instance, the pH and $[CO_3^{2-}]$ estimates of Bartoli et al. (2011) combine to yield glacial-interglacial total alkalinity variations of up ~800 μmol/kg (Figure S5). Such a large change in ocean alkalinity is unlikely over these timescales as alkalinity is stabilized by the distribution of calcium carbonate accumulation and dissolution (carbonate compensation) in the deep sea on scales of thousands of years (Boyle, 1988; Broecker, 1971; Broecker & Peng, 1987). Extrapolating from Last Glacial Maximum (LGM) estimates of alkalinity and lysocline depth, an 800 μmol/kg decrease in alkalinity would

correspond to a >2 km shallower lysocline, which is difficult to reconcile with observations of relatively small changes (<0.5 km) in lysocline depth over the Pleistocene (Farrell & Prell, 1991). Geochemical models also suggest smaller alkalinity adjustments, for example, <400 μmol/kg over the past 10 million years (Figures 3d and 4d of Tyrrell & Zeebe, 2004) and <250 μmol/kg over the past 2.6 Ma (Clark et al., 2006). We therefore revise the PCO_2 record of Bartoli et al. (2011) by using estimates of total alkalinity as the second carbonate system parameter; pH, salinity, and temperature are calculated in the same manner as for Site 668B (sections 2.2 and 2.4). Here alkalinity is calculated via the same regional relationship with salinity that was previously established for Site 999A (Foster, 2008).

$$Total\ Alkalinity_{999A} = 59.19^{*}\ Salinity_{999A} + 229.08. \quad (7)$$

To account for the potential impact of differential weathering on the local alkalinity-to-salinity ratio for these older samples, we increase the alkalinity uncertainty to ±175 μmol/kg for all samples older than 1.8 Ma. Older time periods (>~2 Ma) are less well constrained and so larger uncertainty estimates are used. In contrast to Chalk et al. (2017) who used constant alkalinity and therefore assumed the larger 175 μmol/kg uncertainty throughout, our uncertainty estimates are superimposed on the alkalinity changes based on sea level and are therefore even more conservative than those use by Chalk et al. (2017).

Published boron isotope data are also available from *G. ruber* from Site 999A (Chalk et al., 2017; Foster, 2008; Henehan et al., 2013; Martínez-Botí, Foster et al., 2015; Seki et al., 2010). Boron-based PCO_2 reconstructions from both *T. sacculifer* and *G. ruber* have been extensively calibrated and both species provide convincing PCO_2 estimates compared to ice core records. Here we apply minor revisions to the published $\delta^{11}B_{G.\ ruber}$-based PCO_2 calculations (namely, using a common SST calibration and assuming a constant $\delta^{11}B_{sw}$ over the past 5 Ma) with the goal of ensuring compatible comparisons among the results. All the published $\delta^{11}B_{G.\ ruber}$ values are translated to $\delta^{11}B_{borate}$ using the established species- and instrument-specific calibration of Henehan et al. (2013):

$$\delta^{11}B_{borate} = \left[\delta^{11}B_{G.ruber\ MC-ICP-MS} - 8.87\ (\pm 1.52)\right]/0.60\ (\pm 0.09). \quad (8)$$

In each case, *G. ruber* specimens are from the 300 to 355 μm size fraction so any additional offset for size fraction is not required (Henehan et al., 2013).

The other parameters needed (temperature, salinity, $\delta^{11}B_{sw}$, and alkalinity) are estimated consistently with sections 2.1–2.6. In situ temperature is determined from Mg/Ca values as described by equation (4), except for the record of Seki et al. (2010) in which the alkenone unsaturation index is used for temperature reconstruction as in the original publication; alkenone-based temperatures are indistinguishable from Mg/Ca-based SST at this location. In all cases, salinity is assessed from the modeled sea level estimates of Bintanja and van de Wal (2008), similar to equation (5), with modern salinity of the mixed layer (50 m water depth) at Site 999A of 36.2‰.

$$Salinity_{999A} = 36.2‰ + RMSL/3800\ m^{*}\ 34.8‰. \quad (9)$$

For samples older than 3 Ma, the limit of the RMSL data set (Bintanja & van de Wal, 2008), the oldest value ($S_{t\ =\ 3.0\ Ma}$ = 36.2‰) is used. An alternate method for calculating salinity used by previous publications is via the $\delta^{18}O$ and Mg/Ca values of planktic calcite to find local $\delta^{18}O_{sw}$ and then translate $\delta^{18}O_{sw}$ to a salinity estimate. In practice, this method would result in average salinity ~0.4 lower than estimated above (equation (9)), pH ~0.0002 lower, and PCO_2 ~1 μatm higher. Equations for this alternative salinity estimate can be found in the supporting information.

3. Results

The ODP Site 668B boron-based PCO_2 record for the interval 1.38–1.54 Ma is presented in Figure 3. Within this time period $\delta^{11}B_{T.\ sacculifer}$ values range between a maximum of 22.19 (±0.21)‰ (1.502 Ma) and a minimum of 20.26 (±0.25)‰ (1.402 Ma) with an average $\delta^{11}B$ value of 21.14 (±0.16)‰. Calculated PCO_2 ranges between 183 (±21) μatm (at 1.502 Ma) and 327 (±61) μatm (at 1.408 Ma) with an average PCO_2 value of 258 (±29) μatm. The average amplitude of minimum glacial to maximum interglacial PCO_2 is 92 (±34) μatm (average of four

interglacial maxima [304 (±46) μatm] minus average of five glacial minima [212 (±23) μatm]; these uncertainties are based on the average uncertainty of the data points in question).

The measured $\delta^{11}B_{T.\ sacculifer}$ value is the dominating parameter for the calculated PCO_2 record (Figure S6). To evaluate the respective effects of temperature, alkalinity, and salinity on the calculated PCO_2, we performed a simple sensitivity study in which $\delta^{11}B$ was held constant at the average value (21.15‰), while all other factors (temperature, alkalinity, salinity) varied as evaluated previously. When $\delta^{11}B_{T.\ sacculifer}$ is held constant, the secondary driver of the PCO_2 calculation is local SST, although even the full range of local SST (3.1 K) can only account for a maximum glacial-interglacial PCO_2 range of 24 μatm (Figure S6). Thus, the calculation of paleo-PCO_2 is driven primarily by changes in surface ocean pH as reflected in the raw $\delta^{11}B$ data; temperature, salinity, and alkalinity exert only a minor additional influence on the pH and PCO_2 estimates. This is in contrast to the potentially dominant effects other environmental parameters (i.e., [$B(OH)_4^-$], [HCO_3^-]) can have on B/Ca-based estimates of carbonate parameters (Allen et al., 2012; Tripati et al., 2011).

Published records of $\delta^{11}B$-based PCO_2 were revised to be consistent with the given methodology above. Each parameter revision was tested individually to determine which parameter caused the greatest resulting PCO_2 shift from the original publication. In each instance, *T. sacculifer* $\delta^{11}B$ has been measured via N-TIMS and *G. ruber* $\delta^{11}B$ via MC-ICP-MS. For the longer (0–1.8 Ma) Site 668B *T. sacculifer* data set, average PCO_2 is +2 μatm higher than the published record (Hönisch et al., 2009). This difference is composed of the assumption that $\delta^{11}B_{sw}$ was 39.61‰ rather than 39.5‰ (+6 μatm), the updated $\delta^{11}B_{borate}$ calibration (equation (2), −16 μatm), updated SST calibration (equation (4), +3 μatm), and alkalinity calculated via the constant alkalinity scenario (equation (6), +14 μatm). For Site 999A (0–26 ka), average PCO_2 is also +12 μatm higher than the published record (Henehan et al., 2013), primarily due to the revised salinity and alkalinity estimations (equations (7) and (9)). For Site 999A (0–1.24 Ma), average PCO_2 is +12 μatm higher than the published record (Chalk et al., 2017) also due to the revised salinity and alkalinity estimates. For the Site 999A study of Seki et al. (2010; 0–2.6 Ma), the revised average PCO_2 is +26 μatm higher than the published record (Seki et al., 2010), due to the updated calibration for the boron isotope proxy in *G. ruber* (Henehan et al., 2013). For the Plio-Pleistocene (2.3–3.3 Ma) Site 999A *G. ruber* data set, average PCO_2 is +12 μatm higher than the published record (Martínez-Botí, Marino et al., 2015), primarily due to the revised assumption that seawater $\delta^{11}B_{sw}$ was constant at 39.61‰ over the past 5 Ma (Figure S1), whereas the original publication assumed a lower $\delta^{11}B_{sw}$ (~39.2‰) at the Plio-Pleistocene transition.

For the Plio-Pleistocene (1.97–4.6 Ma) Site 999A *T. sacculifer* data set, average PCO_2 is 41 μatm lower than the published record (Bartoli et al., 2011), primarily due to the revised SST record which omits the depth-based dissolution correction (equation (4), SST 1.8 K cooler, −15 μatm) and the application of the preindustrial disequilibrium value at this site (−21 μatm). The choice of alkalinity, rather than [CO_3^{2-}] as the second parameter of the carbonate system, reduces the glacial-interglacial PCO_2 amplitude of this record by 25% compared to the original publication (Figure S5). This finding highlights the volatile nature of the pH and [CO_3^{2-}] pair in constraining the carbonate system, that is, a small uncertainty in [CO_3^{2-}] translates into a large shift in PCO_2 when paired with pH. The amplitude reduction is a result of both reducing the interglacial PCO_2 estimates and increasing the glacial PCO_2 estimates compared to the original record. All revisions were applied for consistency among calculations; the average PCO_2 change in all cases is smaller than the average 2σ uncertainty reported in the original studies.

4. Discussion

Given that late Pleistocene pCO_2 levels were closely correlated with both tropical SST (e.g., Dyez & Ravelo, 2013; Herbert et al., 2010; Lea, 2004) and high latitude surface temperatures (Jouzel et al., 2007; Petit et al., 1999), an equivalent relationship could be expected for early Pleistocene glacial-interglacial cycles. Here we add to the growing body of data evidence that a similar first-order relationship between global average temperature and pCO_2 also existed in the early Pleistocene, specifically in the interval 1.38–1.54 Ma (Figure 4). During interglacial periods $\delta^{11}B$ was lower (i.e., lower surface ocean pH and higher atmospheric pCO_2) and during glacial periods $\delta^{11}B$ was higher (i.e., higher surface ocean pH and lower atmospheric pCO_2), in line with similar findings for the late Pleistocene period (Chalk et al., 2017; Henehan et al., 2013; Hönisch &

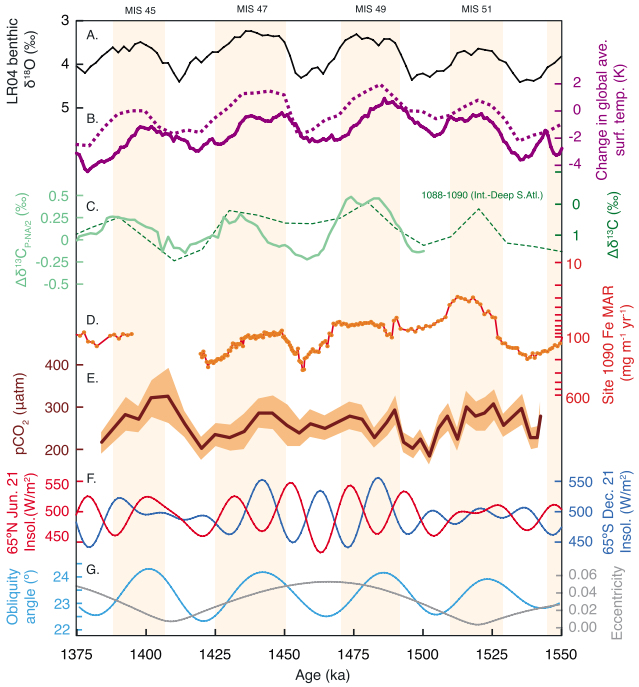

Figure 4. Boron-based pCO_2 record compared with orbital-scale records of the early Pleistocene climate. (a) LR04 benthic oxygen isotope stack (black, Lisiecki & Raymo, 2005) reflects high-latitude temperature and ice volume changes on the dominant ~41-kyr ice age cycle during this interval. (b) Compilations of sea surface temperature records used to estimate change in global average surface temperature (dashed line from Martínez-Botí, Foster et al., 2015, and solid line from *Snyder*, Snyder, 2016). (c) Benthic carbon isotope gradients between Pacific and North Atlantic basins (solid light green line, $\Delta\delta^{13}C_{Pacific\text{-}(North\ Atlantic)/2}$; Lisiecki, 2010) and between intermediate and deep water in the South Atlantic (dashed line; Hodell & Venz-Curtis, 2006). (d) Marine accumulation rate of Fe from ODP Site 1090 (solid line; Martínez-Garcia et al., 2011). (e) Calculated δ^{11}B-based surface ocean pCO_2 from Figure 3. (f, g) Summer insolation at 65°N (blue) and 65°S (red) and orbital parameters (Laskar et al., 2004). MIS = Marine Isotope Stage.

Hemming, 2005). To verify that our data are directly related to variation in atmospheric pCO_2, we need to evaluate a range of processes that could have biased our geochemical signals and interpretations.

First of all, ocean upwelling brings cooler and more CO_2-rich water to the surface; if upwelling had increased during glacial intervals at this location, we would expect to observe a larger glacial-interglacial SST amplitude than other open-ocean sites; if upwelling had increased during interglacial intervals, we would expect a smaller SST amplitude. The local temperature amplitude we measure from Mg/Ca values (i.e., average of four interglacial SST maxima minus average of five glacial SST minima) is 1.4 (±0.3) K, equivalent to other early Pleistocene tropical SST records, whether derived from the south China Sea (Site 1146; 1.4 K, Herbert et al., 2010), the western Pacific (Site 806; 1.2 K, Medina-Elizalde & Lea, 2005; Site 871; 1.2 K, Dyez & Ravelo, 2014), the south Pacific (MD06–3018; 1.3 K, Russon et al., 2010), the tropical Atlantic (Site 662; 1.6 K, Herbert et al., 2010), or the Arabian Sea (Site 722; 1.1 K, Herbert et al., 2010). The similarity of the SST amplitude at Site 668B to other tropical records implies that glacial-interglacial upwelling changes at this site were not substantial and did not preferentially influence either glacial or interglacial δ^{11}B values.

Second, shell diagenesis can occur after shells have been deposited on the ocean floor, potentially biasing our paleoenvironmental interpretations. However, in section 2 we already reasoned against potential dissolution at the sediment surface based on the shallow depth of the core tops and the much deeper Atlantic lysocline. Furthermore, the calcite saturation state of bottom water at this site is Ω_{CaCO3} = 1.5 and bottom water $\Delta[CO_3^{2-}]$ = 34.5, both of which are higher than any site previously used for δ^{11}B-based pCO_2 estimates and above the range suggested for the onset of partial dissolution (Dai et al., 2016; de Villiers, 2005). If diagenesis lowered δ^{11}B values within the buried sediment, we would expect to also observe lower shell weights and higher planktic δ^{18}O and δ^{13}C values (e.g., Edgar et al., 2015). We examined the correlations among these values and do not find any significant relationships to support the notion that diagenesis has occurred within the sediment column. Taken together with the expected range of glacial-interglacial SST presented above, we can reasonably infer that the δ^{11}B-based PCO_2 signal we measure is primary and has not been biased by incomplete preservation.

4.1. Early Pleistocene pCO_2 Varied With Obliquity-Related Climate Cycles

To examine the glacial-interglacial linkages between pCO_2, temperature, and orbital climate parameters from the period 1.38–1.54 Ma, we created cross-plots of reconstructed pCO_2 with physiochemical measurements, orbital parameters, and global stacks of temperature and benthic δ^{18}O (Figure 5). In this analysis, only data that are clearly associated with the broad maxima or minima in temperature and MIS are plotted, as determined by visual comparison with both a benthic δ^{18}O values (Lisiecki & Raymo, 2005) and a global stack of surface temperatures (Snyder, 2016). Omitted are intermediate data that fall between these climate extrema and, due to age model uncertainty, cannot be easily associated with a particular stage; the MIS intervals and maximum/minimum pCO_2 values are listed in Table S2.

With which orbital cycle is pCO_2 most closely related in the early Pleistocene? Cross-plots show that in the late Pleistocene, periods of peak pCO_2 are associated with orbital eccentricity, but in the early Pleistocene peak interglacial pCO_2 is correlated with increased tilt (obliquity) in Earth's rotation axis (Figure 5). The association of pCO_2 and obliquity supports the notion that pCO_2 was linked with the orbital insolation cycle and surface temperatures, even in the 41-kyr world before the MPT, but that the linkages took a different form, which resulted in climate that was in phase with obliquity. This finding is consistent with previously proposed

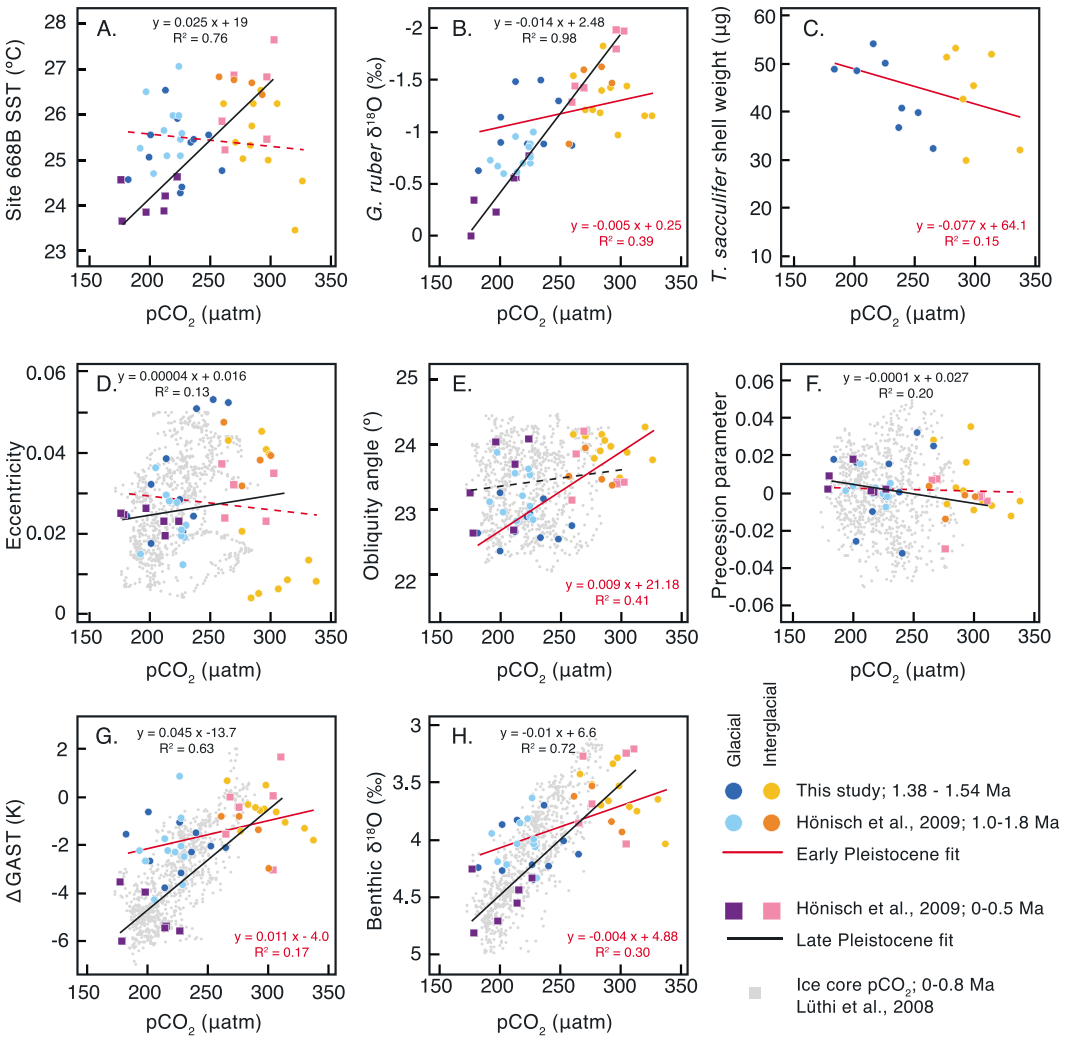

Figure 5. Cross plots of Site 668B peak MIS pCO_2 with Mg/Ca-based SST (a), *G. ruber* $\delta^{18}O$ (b), *T. sacculifer* shell weight (c), coeval orbital parameters (d)–(f) (Laskar et al., 2004), surface temperature (g) and benthic $\delta^{18}O$ (h). Late Pleistocene ice core pCO_2 is plotted for reference in gray (Bereiter et al., 2015), but not used for linear regressions. The linear fit of Early Pleistocene values (circles) is in red, while the linear fit of late Pleistocene values (squares) is in black. Where $R^2 > 0.1$, regression equations are plotted and the linear fit is a solid line. Late Pleistocene pCO_2 is correlated with surface temperature and benthic $\delta^{18}O$, while early Pleistocene pCO_2 is associated with obliquity forcing. Precession parameter is calculated as the standard definition of precession (i.e., where ϖ is the angle between perihelion and vernal equinox on the orbital plane, precession is e*sin(ϖ)). SST = sea surface temperature.

hypotheses for maintaining ~41-kyr periodicity of glacial-interglacial change in the early Pleistocene, either through meridional temperature gradients or ice dynamics. In the early Pleistocene, the 41-kyr cycle could have been promoted by amplified equator-to-pole temperature gradients that carried additional moisture poleward to build ice sheets (Raymo & Nisancioglu, 2003) and/or by thinner, fast-spreading Laurentide ice sheets (Clark et al., 2006). The glacial-interglacial temperature perturbations that drive glacial-interglacial climate would likely have been further amplified by obliquity-scale radiative pCO_2 feedbacks.

4.2. Glacial pCO_2 Decreased Through the Pleistocene

Site 668B $\delta^{11}B_{T.\ sacculifer}$ values indicate that early and late Pleistocene maximum interglacial pCO_2 did not change across the MPT (average interglacial peak pCO_2 at 1.2–1.8 Ma: 303 (±12) µatm, average interglacial peak pCO_2 at 0–0.5 Ma: 299 (±16) µatm; two-tailed t test of all peak interglacial pCO_2 values, $p > 0.7$). However, minimum glacial pCO_2 values declined by ~25 µatm between the early and late Pleistocene (average minimum pCO_2 at 1.2–1.8 Ma: 213 (±10) µatm, average minimum pCO_2 at 0–0.5 Ma: 187 (±10) µatm; two-

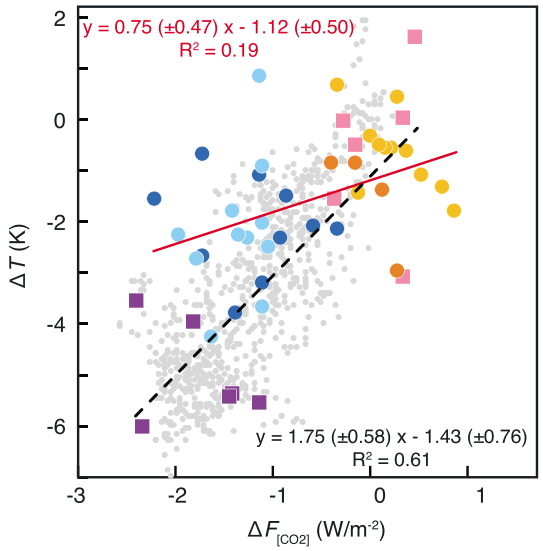

Figure 6. Cross plot of the change in global average surface temperature (ΔT; Snyder, 2016) with the change in radiative pCO_2 forcing ($\Delta F_{[CO2]}$; calculated after Myhre et al., 1998, relative to preindustrial pCO_2 of 278 ppm). Colors are the same as in Figure 5, with fit through early Pleistocene (1.0–1.8 Ma) in red and fit through late Pleistocene data (0–0.8 Ma) in black. Note that this framework considers the contributions of other feedbacks as internal to the Pleistocene climate system.

tailed *t* test of glacial minimum values, $p < 0.05$). These pCO_2 estimates are congruent with proxy records of warmer glacial temperatures in the early Pleistocene than the late Pleistocene and support the initial observation that glacial pCO_2 declined across the MPT (Chalk et al., 2017; Hönisch et al., 2009). While the collapse of North Atlantic deep-water formation around 900 ka coincides with this decrease in glacial pCO_2 (e.g., Pena & Goldstein, 2014), our atmospheric estimates do not allow us to determine the cause of the pCO_2 drawdown. However, the covariation of ocean circulation and pCO_2 shifts over the MPT to longer, colder glacial intervals highlights the close association of ocean dynamics, atmospheric circulation, and climate in the Pleistocene (e.g., Clark et al., 2006).

Glacial pCO_2 was higher in the early Pleistocene than the late Pleistocene, just as glacial temperatures were also 2–2.2 K warmer in the period 1.2–1.8 Ma than in the period 0–0.5 Ma based on multiple compilations of temperature change between the early and late Pleistocene (Herbert et al., 2010; Martínez-Botí, Foster et al., 2015; Snyder, 2016). If average surface temperature is due to the radiative pCO_2 forcing alone, an equilibrium response of global temperature to such forcing can be calculated. At its most basic, this calculation is commonly given in the form of $S_{[CO2]} = \Delta T / \Delta F_{[CO2]}$ where ΔT (change in global average surface temperature) and $\Delta F_{[CO2]}$ (change in radiative forcing due to pCO_2) are millennial-scale averages and all other forcing mechanisms are regarded as internal feedbacks. Here the canonical radiative forcing due to CO_2 is used, where $\Delta F_{[CO2]} = 5.35 * \ln(C/278\ \mu atm)$ and C is atmospheric pCO_2 (Myhre et al., 1998). For the early Pleistocene, we thus calculate an equilibrium temperature response to radiative CO_2 forcing as $S_{[CO2]} = 0.75\ (\pm 0.5)\ °C^{-1} \cdot W^{-1} \cdot m^{-2}$. For the late Pleistocene, the parallel calculation yields $S_{[CO2]} = 1.75\ (\pm 0.6)\ °C^{-1} \cdot W^{-1} \cdot m^{-2}$ (Figure 6). To the first order, these relationships imply that climate sensitivity to radiative greenhouse gas forcing increased by a factor of ~2 between 1.2 and 0.5 Ma, largely driven by lower glacial-interglacial temperature amplitude in the early Pleistocene.

In reality, however, climate feedbacks such as ice sheets and ocean circulation also amplify the range of global average temperature (e.g., Köhler et al., 2015; von der Heydt et al., 2016). Recent studies have pointed out that in order to project the climate effects of rising pCO_2 levels in a warmer world with smaller ice sheets, climate sensitivity must account for the temperature response to each climate parameter separately (i.e., CO_2, ice sheets, etc.; e.g., Köhler et al., 2015; Schmidt et al., 2017). The lower early Pleistocene climate sensitivity calculated above is a result of comparing between time periods in which, at minimum, ice dynamics have changed (Raymo et al., 2006; Shakun et al., 2016). Though this data set does not allow us to quantify changes in albedo and atmospheric circulation, increased glacial ice volume (and vertical growth of ice sheets) at the MPT is an important change in the Earth system that could have amplified glacial-interglacial temperature variability. Increased ice volume cools global temperature through two pathways: by increasing ice sheet extent, which increased global albedo, and through taller ice sheets, which deflected cold northern hemisphere atmospheric jets southward and compressed the subtropical atmospheric bands (Clark et al., 1999; Manabe & Broccoli, 1985; Shinn & Barron, 1989). Qualitatively, then, these additional ice sheet and ocean feedbacks, in conjunction with lower atmospheric pCO_2, worked to cool glacial temperatures across the MPT.

4.3. Model Comparison

We evaluate these reconstructions of early and late Pleistocene pCO_2 with a simple numerical box model that allows for an initial exploration of Pleistocene climate sensitivity given the available surface temperature and pCO_2 data. This model has three coupled components: ice sheets, temperature, and carbon dioxide levels. We force this model with atmospheric insolation over glacial cycles to explore the effect of Laurentide ice sheet changes for climate sensitivity. This model has been documented elsewhere (Schmidt et al., 2017); briefly, this model includes coupling between ice sheet volume (L) and global average surface temperature (T) and between surface temperature and carbon dioxide levels (C) but does not incorporate 3-D geography or

topography. The model is initialized at the following mid-glacial values: T_0 = 285 K, C_0 = 230 μatm, L_0 = −60 m (meters of sea level equivalent). The sensitivity of ice sheets to temperature (a) and the non-Planck feedback (λ) are tested via 20 × 20 experiments (varying a = [0,30] mSL·K^{-1} and λ = [2.8,4.6] W^{-1}·m^{-2}·K^{-1}). These parameters are consistent with the full range of late Pleistocene observations (Köhler et al., 2010).

We use this model to explore the qualitative impact of increasing ice volume on global climate at the MPT. Geochemical evidence and ice sheet models suggest that the Laurentide ice sheet of the early Pleistocene was thinner due to a *slippery* layer of weathered regolith over solid bedrock (Clark et al., 2006; Clark & Pollard, 1998), but that the spatial extent of land ice was similar to the late Pleistocene ice ages (Balco & Rovey, 2010; Roy et al., 2004). Thus, the radiative forcing due to ice sheet albedo was roughly similar in the early and late Pleistocene, but the ice volume required (in equivalent meters of sea level fall) to acquire that forcing was smaller prior to ~1.0 Ma. We test the effect of radiative albedo forcing per ice sheet volume (μ) at 0.025 W^{-1}·m^{-2}·mSL^{-1} for the late Pleistocene such that late Pleistocene ice sheets cooled the global climate by 1 W/m^2 for each 40 m of equivalent sea level fall, consistent with what is assumed for ice-albedo cooling at the LGM (Köhler et al., 2010). If the early Pleistocene Laurentide ice sheet was comparably expansive as in the late Pleistocene, but thinner, it can be thought of as more *efficient* at radiative albedo cooling per unit volume of ice. We investigate this idea by testing the parameter μ (defined above) for the early Pleistocene at double and triple the late Pleistocene value: at 0.05 and 0.075 W^{-1}·m^{-2}·mSL^{-1}. This exercise is not meant to fully simulate the climate system, but to explore elemental system sensitivity to a realistic range of radiative CO_2, insolation, and ice-sheet albedo forcing.

The results of this model suggest that if the efficiency of ice cooling (μ) were higher in the past, the amplitude of temperature variability and atmospheric CO_2 variability would also have been higher. When μ is doubled (or tripled), which simulates the large, but relatively thinner early Pleistocene northern hemisphere ice sheets, temperature and pCO_2 amplitude are ~40 (~80% for tripled μ) larger. However, we do not observe this phenomenon in the early Pleistocene geochemical data sets. Instead, we observe lower temperature variability in the early Pleistocene and a similar amplitude of atmospheric CO_2 variability as in the late Pleistocene. These observations could be a consequence of only considering northern hemisphere insolation and the impact on Laurentide ice. Out-of-phase insolation in the southern hemisphere could have driven Antarctic ice in the opposite direction and dampened overall atmospheric pCO_2 levels by modulating the Southern Ocean dynamics (Raymo et al., 2006). Interhemispheric insolation differences tend to diminish the greater temperature variability that would be implied by greater northern hemisphere ice sheet efficiency in the early Pleistocene.

The simple model described above is also designed to explore the effect of changing Laurentide ice sheet dynamics on climate sensitivity. As the efficiency of ice sheet cooling per unit volume of ice was greater for the early Pleistocene conditions (model μ is increased from 0.025 to 0.075 W^{-1}·m^{-2}·mSL^{-1}) the model suggests that Earth system sensitivity (ESS) must be higher as well. This particular example indicates that a threefold increase in μ would increase ESS from 3.0 to 5.1 K for a doubling of atmospheric CO_2. As stated previously, we observe the opposite in geochemical reconstructions of the early Pleistocene: because the early Pleistocene pCO_2 amplitude is only slightly smaller than the late Pleistocene pCO_2 amplitude, the associated temperature change with a climate sensitivity of 5.1 K per doubling of CO_2 would predict a temperature amplitude of ~4 K. In contrast, we observe a temperature amplitude of ~3 K and a correspondingly lower ESS in the early Pleistocene than in the late Pleistocene. This result simply suggests that Earth's surface temperature in the early Pleistocene is not solely determined by northern hemisphere ice sheets and CO_2 feedbacks. Rather, other forcing factors, which are not explicitly taken into account in this model (e.g., tropical and Southern Ocean dynamics, southern hemisphere insolation, Antarctic ice sheets) must be responsible for helping to dampen glacial-interglacial temperature amplitude in the early Pleistocene.

4.4. Species-Specific Differences; Implications for Plio-Pleistocene pCO_2 Drawdown

As the boron isotope proxy gains maturity and acceptance in the scientific community, the number of δ^{11}B-based data sets has increased, offering an opportunity to glean more detailed insight into the interplay between pCO_2 and climate. In Figure 7 we compile new pCO_2 estimates alongside ice-core records of late Pleistocene pCO_2 (Bereiter et al., 2015; Higgins et al., 2015) and six published records of δ^{11}B-based pCO_2. As described above, the δ^{11}B-based pCO_2 data (Bartoli et al., 2011; Chalk et al., 2017; Henehan et al., 2013;

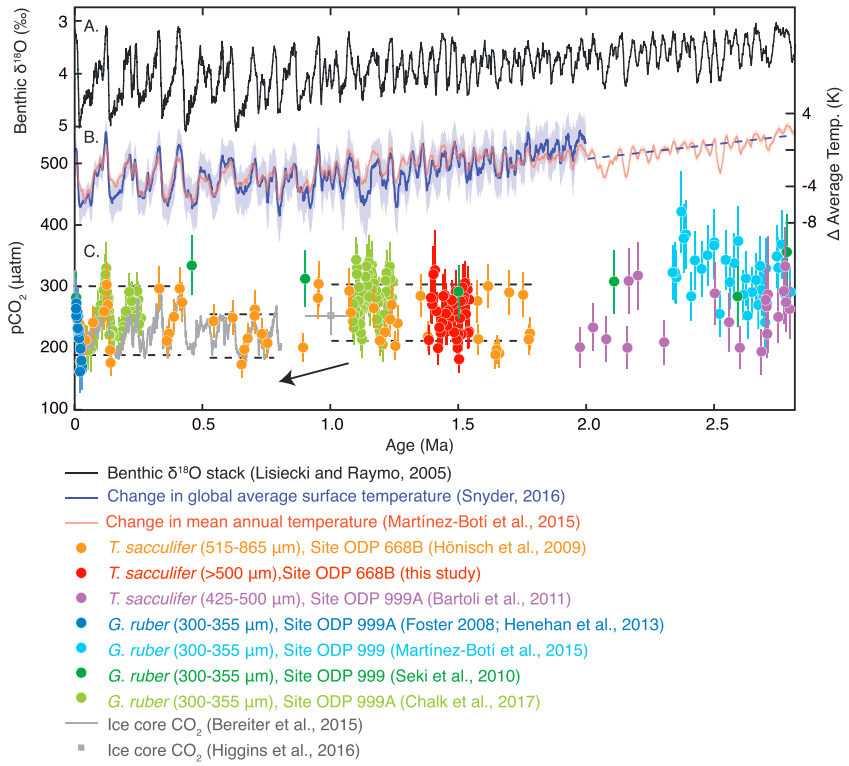

Figure 7. (a) Benthic $\delta^{18}O$ (Lisiecki & Raymo, 2005) and (b) change in global average surface temperature (ΔGAST; Snyder, 2016) compared with (c) pCO_2 derived from ice cores (Bereiter et al., 2015; Higgins et al., 2015) and boron isotope reconstructions (Bartoli et al., 2011; Chalk et al., 2017; Henehan et al., 2013; Hönisch et al., 2009; Martínez-Botí, Foster et al., 2015; Seki et al., 2010). Published pCO_2 records have been recalculated using consistent methods (see section 2) from the original $\delta^{11}B$ data. Late Pleistocene boron-based pCO_2 records from Sites 999A and 668B are in the same range as ice-core-based pCO_2 measurements. The largest resulting difference is the record of Bartoli et al. (2011), to which new temperature data have been applied and pCO_2 is calculated by pairing pH with alkalinity estimates rather than $[CO_3^{2-}]$. ODP = Ocean Drilling Program.

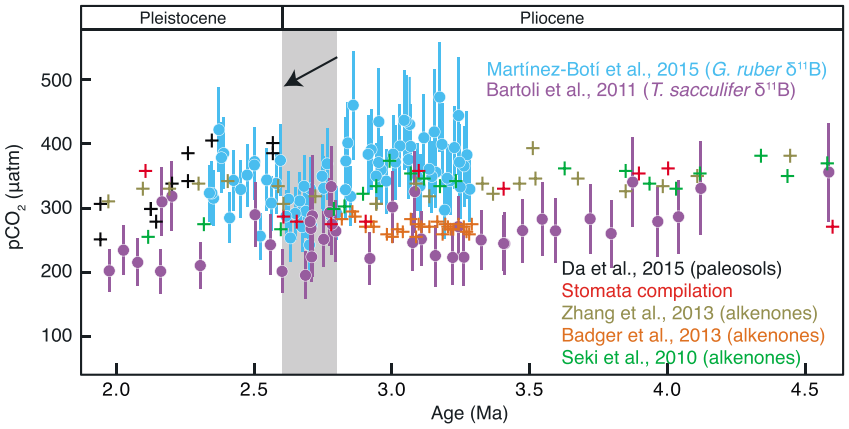

Figure 8. Revised pCO_2 values using $\delta^{11}B$ from *T. sacculifer* (Bartoli et al., 2011; purple) compared with pCO_2 from *G. ruber* (Martínez-Botí, Foster et al., 2015; blue). In the interval 2.8–2.6 Ma, *G. ruber*-based pCO_2 declines by >100 µatm, coincident with the onset of northern hemisphere glaciation (gray band, black arrow). Throughout the Pliocene, the *T. sacculifer*-based pCO_2 record is lower than *G. ruber*-based pCO_2 but also shifts to lower values at 2.7 Ma. The text discusses potential offsets due to evolutionary changes in foraminiferal physiology and consequent species-differences between pH and pCO_2 reconstructions. Paleo-pCO_2 reconstructions from paleosols (Da et al., 2015), stomatal indices (Kürschner et al., 1996; Retallack, 2009; Stults et al., 2011; Wang et al., 2015), and alkenone $\delta^{13}C$ (Badger et al., 2013; Seki et al., 2010; Zhang et al., 2013) are intermediate between the estimates of Martínez-Botí, Foster et al. (2015) and Bartoli et al. (2011).

Hönisch et al., 2009; Martínez-Botí, Foster et al., 2015; Seki et al., 2010) have been recalculated to minimize differences in the chemical and physical boundary conditions estimated for each record (see section 2.7). It is worth reiterating that the resulting pCO_2 values are primarily dependent on the published $\delta^{11}B$ measurements and that our minor revisions in boundary condition treatment do not shift average pCO_2 estimates outside of the published 2σ uncertainty bands.

Paleo-pCO_2 estimates based on $\delta^{11}B$ values of either *T. sacculifer* or *G. ruber* (Bartoli et al., 2011; Martínez-Botí, Foster et al., 2015) suggest that pCO_2 declined by 50–100 μatm between 2.8 and 2.6 Ma (Figure 8). This pCO_2 drawdown, coincident with the onset of northern hemisphere glaciation (Haug et al., 1999; Raymo, 1994), is thought to be the result of increased glacial dust load and greater biological productivity in high-nitrate low-chlorophyll regions (Bailey et al., 2011) or polar stratification which sequestered carbon in the deep ocean in both the north Pacific (e.g., Haug et al., 1999; Sigman et al., 2004) and the Southern Ocean (Hodell & Venz-Curtis, 2006; Martínez-Garcia et al., 2011; Waddell et al., 2009). The pCO_2 initial drawdown at 2.8–2.6 Ma is implicated in the increased glaciation of Greenland and the northern hemisphere more broadly (Lunt et al., 2008).

Nonetheless, a distinct mismatch exists between the two $\delta^{11}B$-based pCO_2 estimates from Site 999A (Figures 7 and 8) for much of the late Pliocene. Where these two records overlap (from 3.3 to 2.3 Ma), the *G. ruber*-based pCO_2 estimates are on average 90 μatm higher than the *T. sacculifer* estimates (Figures 7 and 8). This difference is apparent to a small degree even where *G. ruber* and *T. sacculifer* records overlap in the late Pleistocene, and as a mismatch between *G. ruber* and ice core records (Figure S8), although the species difference is larger further back in time. We can rule out discrepancies in environmental temperature as impacting the equilibrium constants because the Mg/Ca-based temperature reconstructions from the two data sets are indistinguishable (Figure S7b). As we have already precluded inconsistent treatment of the physicochemical boundary conditions, the difference is more likely rooted in the underlying $\delta^{11}B$ data of *G. ruber* and *T. sacculifer*, where $\delta^{11}B_{G.\ ruber}$ decreases more strongly between the last glacial cycle and the late Pliocene than $\delta^{11}B_{T.\ sacculifer}$. It is important to explore this discrepancy, which could be explained a biologically mediated shift in the $\delta^{11}B_{calcite}$ to $\delta^{11}B_{borate}$ calibration (Figure S9), as differential pCO_2 results have important implications for Plio-Pleistocene climate research (e.g., Martínez-Botí, Foster et al., 2015).

Differences in the pCO_2 reconstructions from these two surface dwelling foraminifera could in theory result from diagenetic alteration or incomplete sample cleaning. However, in the specific case of the late Pliocene data, evaluation of these factors is partly constrained by the fact that both species have been analyzed from the same sediment core. The first of these arguments relates to the potential bias due to partial dissolution, which typically lowers the $\delta^{11}B$ value by preferential removal of higher-$\delta^{11}B$ calcite (e.g., Hönisch & Hemming, 2004). Both Pliocene data sets were measured using material from the same shallow core, so diagenetic alteration due to regional changes in the lysocline can reasonably be excluded. Could dissolution susceptibility be species-specific (e.g., Berger, 1967)? Higher pCO_2 estimates are based on lower $\delta^{11}B$ values, suggesting that *G. ruber* would have to be more dissolved than *T. sacculifer*. Shell-weight evidence indeed suggests that *G. ruber* is slightly more susceptible to partial dissolution than *T. sacculifer* based on in situ and laboratory work (e.g., Thunell & Honjo, 1981). In actuality, however, studies of foraminiferal $\delta^{11}B$ from depth transects have suggested that *G. ruber* $\delta^{11}B$ values may be more robust and not greatly affected by partial dissolution (Henehan et al., 2013; Ni et al., 2007; Seki et al., 2010) and that the foraminiferal $\delta^{11}B$ signature is preserved even when the shell is visibly recrystallized (Edgar et al., 2015). Another factor which could lower $\delta^{11}B$ values is contamination from pelagic clays, whose $\delta^{11}B$ values typically fall in the -7 to +5‰ range (Ishikawa & Nakamura, 1993) and are thus much lower than $\delta^{11}B$ of foraminiferal calcite. For the *G. ruber* pCO_2 estimates to agree with the *T. sacculifer* estimates, clay contamination would have to explain the -1‰ discrepancy in $\delta^{11}B_{G.\ ruber}$. This would require the *G. ruber* samples to have contained ~5 wt % clay, which is unlikely given the robust cleaning protocol applied to remove impurities and the careful contaminant screening for aluminum and iron (e.g., Chalk et al., 2017; Martínez-Botí, Foster et al., 2015).

At this point we have reasonably ruled out dissolution differences and clay contamination in addition to differential temperature calibrations, $\delta^{11}B_{sw}$ values, salinity, and alkalinity estimates. It is therefore more likely that the difference is biological. Although both foraminifera species and instrumental techniques have been calibrated using modern cultured and core top specimens and shown to replicate the ice-core pCO_2 record of the last glacial cycle (Chalk et al., 2017; Foster, 2008; Henehan et al., 2013; Hönisch & Hemming, 2004, 2005),

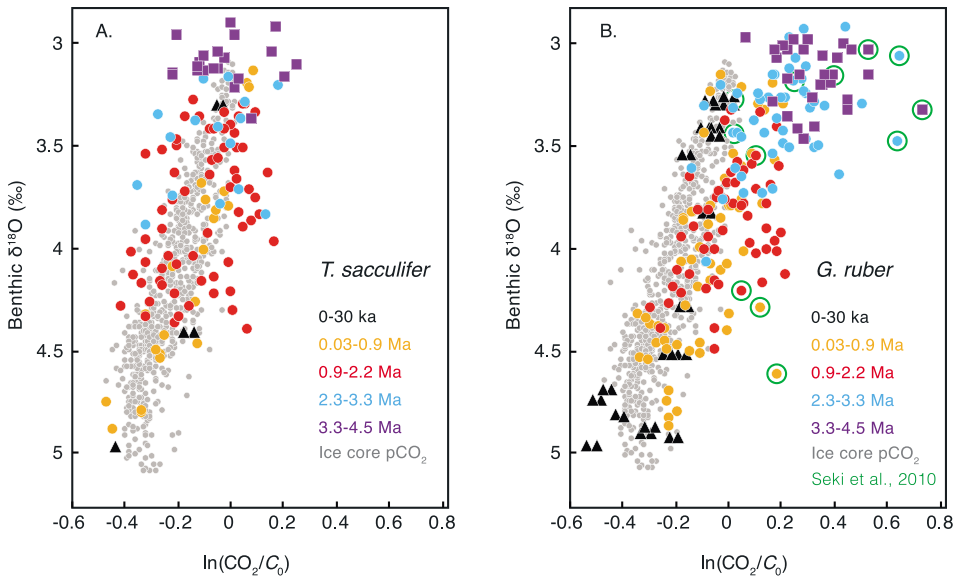

Figure 9. Relationship between benthic $\delta^{18}O$ and climate forcing due to radiative CO_2 forcing (ln (CO_2/C_0), where C_0 is 278 μatm), including all six $\delta^{11}B$-based pCO_2 records presented in Figure 7. (a) Forcing derived from $\delta^{11}B_{T.\ sacculifer}$-based pCO_2 compared with forcing from pCO_2 values derived from ice cores (gray). Time periods are coded by color, yet the overall benthic $\delta^{18}O$-to-ln (CO_2/C_0) relationship for boron-based pCO_2 data falls along the same relationship for pCO_2 as that derived from ice cores. (b) The corresponding relationship of boron-based CO_2 forcing compared with pCO_2 values from ice cores, this time using $\delta^{11}B$ values from *G. ruber*. Although Holocene and LGM pCO_2 values based on the foraminifer *G. ruber* are consistent with the ice-core pCO_2, the estimates deviate in earlier time periods, when pCO_2 values are higher than expected based on the general benthic $\delta^{18}O$: Ln (CO_2/C_0) relationship derived from ice cores. This gives rise to the question of whether *G. ruber* and its vital effects evolved over time. Values derived from one early study are circled in green; these data are based on unusually low boron isotope values (Seki et al., 2010).

one or both of the studied foraminifer species could have evolved prior to the last glacial cycle. One line of evidence for such an evolutionary shift has been described by Bartoli et al. (2011), who could not find enough Pliocene *T. sacculifer* specimens in the >500 μm test size fraction and instead substituted specimens in the 425–500 μm range. Hönisch and Hemming (2004) observed no significant difference in $\delta^{11}B_{T.\ sacculifer}$ between the 425–500 and >500 μm test size fraction, suggesting that the depth habitat and ecology is the same for both of the large size fractions. Indeed, if the overall smaller specimens of the largest size fraction in the early Pleistocene sediments had inhabited a deeper water depth, *T. sacculifer* should have recorded lower $\delta^{11}B$, which would imply lower pH and elevated pCO_2. Instead, we observe the opposite pattern: *T. sacculifer* pCO_2 estimates are lower than those based on *G. ruber* (Chalk et al., 2017; Martínez-Botí, Foster et al., 2015; Seki et al., 2010).

Could the response of *G. ruber* to ocean pH have evolved over the Plio-Pleistocene? Interestingly, in the modern Caribbean the pink variety of *G. ruber* is quite abundant, whereas the culture and global core top calibration of Henehan et al. (2013) is based on the white variety. The canonical *G. ruber* morphospecies represents up to five genetically distinct varieties each with nonunique ecological and biogeographic preferences. In contrast, *T. sacculifer* does not exhibit such cryptic diversity (André et al., 2012; Darling & Wade, 2008). Confidence in the $\delta^{11}B$ proxy of pCO_2 in the Pliocene and early Pleistocene is strengthened by good proxy replication of pCO_2 with the ice core record (past 800 ka). In comparing the last two glacial cycles, average *G. ruber* $\delta^{11}B$ values are ~0.3‰ lower in MIS 6 even as pCO_2 derived from ice cores is nearly identical in MIS 2 and 6 (Chalk et al., 2017). Using a consistent method for estimating temperature, in this case via Evans and Müller (2012), the pCO_2 calculated from *G. ruber* $\delta^{11}B$ is ~40 μatm higher in MIS 6 than in MIS 2. This result suggests that evolutionary differences in *G. ruber* could be as young as ~200 ka. Once again, the Mg/Ca-based temperatures derived from these two species do not diverge in the Plio-Pleistocene (3.3–2.3 Ma), which implies that the difference in reconstructed pCO_2 is less likely due to changes in habitat depth or seasonal preferences.

Finally, pCO_2 estimates from other proxy archives are at odds with the highest Pliocene *G. ruber*-based pCO_2 estimates (Figure 8). For example, evidence from the alkenone $\delta^{13}C$ proxy suggests lower (<350 μatm) levels of late Pliocene pCO_2, whether derived from Site 999A, (high resolution data: 270 ± 40; Badger et al., 2013), (low resolution data: 330 ± 40; Seki et al., 2010), or from Site 925 in eastern tropical Atlantic (320 ± 40; Zhang et al., 2013). While different proxies have different uncertainties, the larger amplitude of Pliocene pCO_2 change in the *G. ruber*-based record (~150 μatm as opposed to ~100 μatm in the *T. sacculifer*-based record) is difficult to justify given the smaller amplitude of glacial-interglacial cycles in the Pliocene (Lisiecki & Raymo, 2005). In summary, although we cannot unequivocally state which species may have changed behavior, it will be important to cross-calibrate the $\delta^{11}B$ proxy in the Pliocene with regard to potential physiological distinctions.

Importantly, both *G. ruber* and *T. sacculifer* record a pCO_2 decline through the Plio-Pleistocene (Figures 7 and 8), but the extent of the pCO_2 decline is larger for *G. ruber* reconstructions and this has critical implications for estimates of climate sensitivity from these two species. If the Pliocene *G. ruber*-based pCO_2 estimate is correct, then late Pliocene (3.3–2.8 Ma) pCO_2 levels were relatively high (>350 μatm), and highly variable, and then dramatically declined at the onset of northern hemisphere glaciation. Martínez-Botí, Foster et al. (2015) use this data to infer low sensitivity to radiative pCO_2 forcing in the Pliocene and higher sensitivity in the Pleistocene. They call out increased continental ice-albedo as the primary mechanism for this change in sensitivity and use, as one line of evidence, the inflection point at ~275 μatm in the relationship between benthic $\delta^{18}O$ and forcing due to pCO_2 changes (Martínez-Botí, Foster et al., 2015). Here we replot this figure using all available data sets discussed herein, but we also separate the two species (Figure 9). Martínez-Botí, Foster et al. (2015) originally excluded the data of Bartoli et al. (2011) from their plot to improve clarity, but it now emerges that the change in slope of the relationship observed by Martínez-Botí, Foster et al. (2015) is only true for *G. ruber* but not for *T. sacculifer* (Figure 9). Explaining the larger Plio-Pleistocene CO_2 drawdown inferred by the *G. ruber* $\delta^{11}B$ record requires significant increases in ocean stratification, dust fertilization, and/or (potentially) silicate rock weathering since the Pliocene (e.g., Martínez-Garcia et al., 2011).

If, on the other hand, the Pliocene *T. sacculifer*-based pCO_2 estimates are correct, Pliocene pCO_2 was less elevated relative to early Pleistocene pCO_2 values and the linear relationship between benthic $\delta^{18}O$ and pCO_2 forcing extended into the Pliocene (Figure 9a). The *T. sacculifer*-based estimates, with pCO_2 likely <350–400 μatm, support the evidence for lower Pliocene pCO_2 from other proxies (Figure 8): alkenone $\delta^{13}C$, stomatal indices, and paleosols (e.g., Badger et al., 2013; Da et al., 2015; Wang et al., 2015) and implies that atmospheric pCO_2 was relatively similar between the late Pliocene and early Pleistocene, despite the descent into cooler polar temperatures. If correct, this record implies that Arctic temperatures declined at the Plio-Pleistocene transition due to factors other than direct radiative pCO_2 forcing, such as the thickening of northern hemisphere ice sheets or reduced poleward oceanic heat transport. Further work is warranted to improve our understanding of foraminiferal vital effects on $\delta^{11}B$, and thereby improve confidence in paleo-pCO_2 estimates from this proxy.

5. Conclusions

Glacial-interglacial climate cycles in the early Pleistocene (>1 Ma) were shorter and less severe than the iconic 100-kyr cycles of the last 0.5 million years. Our new high-resolution record of atmospheric pCO_2 over three glacial cycles in the early Pleistocene (1.38–1.54 Ma) is closely linked with obliquity pacing, with an average pCO_2 amplitude of 92 (±13) μatm. Over the MPT, glacial pCO_2 declined, alongside glacial SST cooling in both the tropics and high latitudes. In contrast to an earlier assessment of climate sensitivity from $\delta^{11}B$ in *G. ruber*, our compilation of pCO_2 estimates from $\delta^{11}B$ in *T. sacculifer* suggests apparent climate sensitivity in the early Pleistocene was lower compared to the late Pleistocene; the difference is likely due to changing ocean or ice sheet dynamics over the mid-Pleistocene. Using a simple model, we suggest that the lower climate sensitivity in the early Pleistocene was not directly related to the thinner, yet extensive, northern hemisphere terrestrial ice sheets, but is rather a result of changing ocean dynamics in the southern hemisphere or tropics. The observed discrepancy in late Pliocene pCO_2 estimates based on *G. ruber* and *T. sacculifer* requires further study of potentially evolving species-specific vital effects in the past, so that paleo-pCO_2 estimates from the proxy can be appreciated with confidence.

Acknowledgments
We thank the International Ocean Drilling Program repository for providing samples for these analyses and Carina Fish, Peter deMenocal, and Angela Dial for assistance with the new trace element analyses. This work was funded by the National Science Foundation grant EAR-1349616 to K.D. and a gift from Gerry Lenfest to B.H. Upon publication, all original data from this study will be archived at NOAA's National Center for Environmental Information at https://www.ncdc.noaa.gov/paleo/study/25490 as a part of the Research Coordination Network grant to B.H. and Pratigya Polissar (OCE 16-36005).

References

Allen, K. A., Hönisch, B., Eggins, S. M., & Rosenthal, Y. (2012). Environmental controls on B/Ca in calcite tests of the tropical planktic foraminifer species *Globigerinoides ruber* and *Globigerinoides sacculifer*. *Earth and Planetary Science Letters*, *351-352*(C), 270–280. https://doi.org/10.1016/j.epsl.2012.07.004

Anand, P., Elderfield, H., & Conte, M. H. (2003). Calibration of Mg/Ca thermometry in planktonic foraminifera from a sediment trap time series. *Paleoceanography*, *18*(2), 1050. https://doi.org/10.1029/2002PA000846

Anderson, R. F., Ali, S., Bradtmiller, L. I., Nielsen, S., Fleisher, M. Q., Anderson, B. E., & Burckle, L. H. (2009). Wind-driven upwelling in the Southern Ocean and the deglacial rise in atmospheric CO_2. *Science*, *323*(5920), 1443–1448. https://doi.org/10.1126/science.1167441

André, A., Weiner, A., Quillévéré, F., Aurahs, R., Morard, R., Douady, C. J., et al. (2012). The cryptic and the apparent reversed: lack of genetic differentiation within the morphologically diverse plexus of the planktonic foraminifer Globigerinoides sacculifer. *Paleobiology*, *39*(1), 21–39. https://doi.org/10.1666/0094-8373-39.1.21

Badger, M. P. S., Schmidt, D. N., Mackensen, A., & Pancost, R. D. (2013). High-resolution alkenone palaeobarometry indicates relatively stable pCO_2 during the Pliocene (3.3-2.8 Ma). *Philosophical Transactions of the Royal Society A: Mathematical, Physical and Engineering Sciences*, *70*(15), 3883–3904. https://doi.org/10.1016/j.gca.2006.06.009

Bailey, I., Liu, Q., Swann, G. E. A., Jiang, Z., Sun, Y., Zhao, X., & Roberts, A. P. (2011). Iron fertilisation and biogeochemical cycles in the sub-Arctic northwest Pacific during the late Pliocene intensification of northern hemisphere glaciation. *Earth and Planetary Science Letters*, *307*(3–4), 253–265. https://doi.org/10.1016/j.epsl.2011.05.029

Balco, G., & Rovey, C. W. (2010). Absolute chronology for major Pleistocene advances of the Laurentide ice sheet. *Geology*, *38*(9), 795–798. https://doi.org/10.1130/G30946.1

Barker, S., Greaves, M., & Elderfield, H. (2003). A study of cleaning procedures used for foraminiferal Mg/Ca paleothermometry. *Geochemistry, Geophysics, Geosystems*, *4*(9), 8407. https://doi.org/10.1029/2003GC000559

Bartoli, G., Hönisch, B., & Zeebe, R. E. (2011). Atmospheric CO_2 decline during the Pliocene intensification of northern hemisphere glaciations. *Paleoceanography*, *26*, PA3206. https://doi.org/10.1029/2010PA002055

Bé, A. W. H. (1980). Gametogenic calcification in a spinose planktonic foraminifer, *Globigerinoides sacculifer* (Brady). *Marine Micropaleontology*, *5*, 283–310. https://doi.org/10.1016/0377-8398(80)90014-6

Bemis, B. E., Spero, H. J., Bijma, J., & Lea, D. W. (1998). Reevaluation of the oxygen isotopic composition of planktonic foraminifera: Experimental results and revised paleotemperature equations. *Paleoceanography*, *13*(2), 150–160. https://doi.org/10.1029/98PA00070

Bereiter, B., Eggleston, S., Schmitt, J., Nehrbass-Ahles, C., Stocker, T. F., Fischer, H., et al. (2015). Revision of the EPICA Dome C CO2 record from 800 to 600kyr before present. *Geophysical Research Letters*, *42*, 542–549. https://doi.org/10.1002/2014GL061957

Berger, W. H. (1967). Foraminiferal ooze: Solution at depths. *Science*, *156*(3773), 383–385. https://doi.org/10.1126/science.156.3773.383

Bibby, T., Putkonen, J., Morgan, D., Balco, G., & Shuster, D. L. (2016). Million year old ice found under meter thick debris layer in Antarctica. *Geophysical Research Letters*, *43*, 6995–7001. https://doi.org/10.1002/2016GL069889

Bintanja, R., & van de Wal, R. S. W. (2008). North American ice-sheet dynamics and the onset of 100,000-year glacial cycles. *Nature*, *454*(7206), 869–872. https://doi.org/10.1038/nature07158

Bird, M. I., & Cali, J. A. (1998). A million-year record of fire in sub-Saharan Africa. *Nature*, *394*(6695), 767–769. https://doi.org/10.1038/29507

Bird, M. I., & Cali, J. A. (2002). A revised high-resolution oxygen-isotope chronology for ODP-668B: Implications for Quaternary biomass burning in Africa. *Global and Planetary Change*, *33*(1–2), 73–76. https://doi.org/10.1016/S0921-8181(02)00062-0

Boyle, E. A. (1988). The role of vertical chemical fractionation in controlling Late Quaternary atmospheric carbon-dioxide. *Journal of Geophysical Research*, *93*(C12), 15,701–15,714. https://doi.org/10.1029/JC093iC12p15701

Boyle, E. A., & Keigwin, L. D. (1985). Comparison of Atlantic and Pacific paleochemical records for the last 215,000 years: Changes in deep ocean circulation and chemical inventories. *Earth and Planetary Science Letters*, *76*(1–2), 135–150. https://doi.org/10.1016/0012-821X(85)90154-2

Branson, O., Kaczmarek, K., Redfern, S. A. T., Misra, S., Langer, G., Tyliszczak, T., et al. (2015). The coordination and distribution of B in foraminiferal calcite. *Earth and Planetary Science Letters*, *416*(C), 67–72. https://doi.org/10.1016/j.epsl.2015.02.006

Brennan, S. T., Lowenstein, T. K., & Cendon, D. I. (2013). The major-ion composition of Cenozoic seawater: The past 36 million years from fluid inclusions in marine halite. *American Journal of Science*, *313*(8), 713–775. https://doi.org/10.2475/08.2013.01

Broecker, W. S. (1971). Calcite accumulation rates and glacial to interglacial changes in oceanic mixing. In K. K. Turekian (Ed.), *The Late Cenozoic glacial ages* (pp. 239–265). New Haven: Yale University.

Broecker, W. S., & Peng, T.-H. (1987). The role of $CaCO_3$ compensation in the glacial to interglacial atmospheric CO_2 change. *GBC*, *1*(1), 15–29. https://doi.org/10.1029/GB001i001p00015

Chalk, T. B., Hain, M. P., Foster, G. L., Rohling, E. J., Sexton, P. F., Badger, M. P. S., et al. (2017). Causes of ice age intensification across the mid-Pleistocene transition. *PNAS*, *114*(50), 13,114–13,119. https://doi.org/10.1073/pnas.1702143114

Clark, P. U., Alley, R. B., & Pollard, D. (1999). Northern hemisphere ice-sheet influences on global climate change. *Science*, *286*(5442), 1104–1111. https://doi.org/10.1126/science.286.5442.1104

Clark, P. U., Archer, D., Pollard, D., Blum, J. D., Rial, J. A., Brovkin, V., et al. (2006). The middle Pleistocene transition: Characteristics, mechanisms, and implications for long-term changes in atmospheric pCO_2. *Quaternary Science Reviews*, *25*(23–24), 3150–3184. https://doi.org/10.1016/j.quascirev.2006.07.008

Clark, P. U., & Pollard, D. (1998). Origin of the middle Pleistocene transition by ice sheet erosion of regolith. *Paleoceanography*, *13*(1), 1–9. https://doi.org/10.1029/97pa02660

Da, J., Zhang, Y. G., Wang, H., Balsam, W., & Ji, J. (2015). An Early Pleistocene atmospheric CO_2 record based on pedogenic carbonate from the Chinese loess deposits. *Earth and Planetary Science Letters*, *426*(C), 69–75. https://doi.org/10.1016/j.epsl.2015.05.053

Dai, Y., Yu, J., & Johnstone, H. J. H. (2016). Distinct responses of planktonic foraminiferal B/Ca to dissolution on seafloor. *Geochemistry, Geophysics, Geosystems*, *17*, 1339–1348. https://doi.org/10.1002/2015GC006199

Darling, K. F., & Wade, C. M. (2008). The genetic diversity of planktic foraminifera and the global distribution of ribosomal RNA genotypes. *Marine Micropaleontology*, *67*(3-4), 216–238. https://doi.org/10.1016/j.marmicro.2008.01.009

de Villiers, S. (2005). Foraminiferal shell-weight evidence for sedimentary calcite dissolution above the lysocline. *Deep Sea Research Part I: Oceanographic Research Papers*, *52*(5), 671–680. https://doi.org/10.1016/j.dsr.2004.11.014

Dekens, P. S., Lea, D. W., Pak, D. K., & Spero, H. J. (2002). Core top calibration of Mg/Ca in tropical foraminifera: Refining paleotemperature estimation. *Geochemistry, Geophysics, Geosystems*, *3*(4), 1022. https://doi.org/10.1029/2001GC000200

Delaney, M. L., Bé, A. W. H., & Boyle, E. A. (1985). Li, Sr, Mg, and Na in foraminiferal calcite shells from laboratory culture, sediment traps, and sediment cores. *Geochimica et Cosmochimica Acta*, *49*, 1327–1341. https://doi.org/10.1016/0016-7037(85)90284-4

Dickson, A. G. (1990). Thermodynamics of the dissociation of boric acid in synthetic seawater from 273.15 to 318.15 K. *Deep Sea Research, Part II*, *35*, 253–257. https://doi.org/10.1021/je00061a009

Dyez, K., & Ravelo, A. C. (2013). Late Pleistocene tropical Pacific temperature sensitivity to radiative greenhouse gas forcing. *Geology*, *41*(1), 23–26. https://doi.org/10.1130/G33425.1

Dyez, K., & Ravelo, A. C. (2014). Dynamical changes in the tropical Pacific warm pool and zonal SST gradient during the Pleistocene. *Geophysical Research Letters*, *41*, 7626–7633. https://doi.org/10.1002/2014GL061639

Edgar, K. M., Anagnostou, E., Pearson, P. N., & Foster, G. L. (2015). Assessing the impact of diagenesis on $\delta^{11}B$, $\delta^{13}C$, $\delta^{18}O$, Sr/Ca and B/Ca values in fossil planktic foraminiferal calcite. *Geochimica et Cosmochimica Acta*, *166*(C), 189–209. https://doi.org/10.1016/j.gca.2015.06.018

Evans, D., Brierley, C. M., Raymo, M. E., Erez, J., & Müller, W. (2016). Planktic foraminifera shell chemistry response to seawater chemistry: Pliocene–Pleistocene seawater Mg/Ca, temperature and sea level change. *Earth and Planetary Science Letters*, *438*(C), 139–148. https://doi.org/10.1016/j.epsl.2016.01.013

Evans, D., & Müller, W. (2012). Deep time foraminifera Mg/Ca paleothermometry: Nonlinear correction for secular change in seawater Mg/Ca. *Paleoceanography*, *27*, PA4205. https://doi.org/10.1029/2012PA002315

Fantle, M. S., & DePaolo, D. J. (2005). Variations in the marine Ca cycle over the past 20 million years. *Earth and Planetary Science Letters*, *237*(1–2), 102–117. https://doi.org/10.1016/j.epsl.2005.06.024

Fantle, M. S., & DePaolo, D. J. (2006). Sr isotopes and pore fluid chemistry in carbonate sediment of the Ontong Java Plateau: Calcite recrystallization rates and evidence for a rapid rise in seawater Mg over the last 10 million years. *Geochimica et Cosmochimica Acta*, *70*(15), 3883–3904. https://doi.org/10.1016/j.gca.2006.06.009

Farmer, E. C., Kaplan, A., de Menocal, P. B., & Lynch-Stieglitz, J. (2007). Corroborating ecological depth preferences of planktonic foraminifera in the tropical Atlantic with the stable oxygen isotope ratios of core top specimens. *Paleoceanography*, *22*, PA3205. https://doi.org/10.1029/2006PA001361

Farmer, J. R., Hönisch, B., & Uchikawa, J. (2016). Single laboratory comparison of MC-ICP-MS and N-TIMS boron isotope analyses in marine carbonates. *Chemical Geology*, *447*, 173–182. https://doi.org/10.1016/j.chemgeo.2016.11.008

Farrell, J. W., & Prell, W. L. (1991). Pacific CaCO3 preservation and δ18O since 4 Ma: Paleoceanic and Paleoclimatic implications. *Paleoceanography*, *6*(4), 485–498. https://doi.org/10.1029/91PA00877

Fischer, H., Schmitt, J., Lüthi, D., Stocker, T. F., Tschumi, T., Parekh, P., et al. (2010). The role of Southern Ocean processes in orbital and millennial CO_2 variations—A synthesis. *Quaternary Science Reviews*, *29*(1–2), 193–205. https://doi.org/10.1016/j.quascirev.2009.06.007

Fischer, H., Severinghaus, J., Brook, E., Wolff, E., Albert, M., Alemany, O., et al. (2013). Where to find 1.5 million yr old ice for the IPICS "Oldest Ice" ice core. *Climate of the Past Discussions*, *9*(3), 2771–2815. https://doi.org/10.5194/cpd-9-2771-2013

Foster, G. L. (2008). Seawater pH, pCO_2 and $[CO_3^{-2}]$ variations in the Caribbean Sea over the last 130 kyr: A boron isotope and B/Ca study of planktic foraminifera. *Earth and Planetary Science Letters*, *271*(1–4), 254–266. https://doi.org/10.1016/j.epsl.2008.04.015

Foster, G. L., Hönisch, B., Paris, G., Dwyer, G. S., Rae, J. W. B., Elliott, T., et al. (2013). Interlaboratory comparison of boron isotope analyses of boric acid, seawater and marine $CaCO_3$ by MC-ICPMS and NTIMS. *Chemical Geology*, *358*(C), 1–14. https://doi.org/10.1016/j.chemgeo.2013.08.027

Foster, G. L., Pogge von Strandmann, P. A. E., & Rae, J. W. B. (2010). Boron and magnesium isotopic composition of seawater. *Geochemistry, Geophysics, Geosystems*, *11*, Q08015. https://doi.org/10.1029/2010GC003201

Gloor, M., Gruber, N., Sarmiento, J., Sabine, C. L., Feely, R. A., & Rödenbeck, C. (2003). A first estimate of present and preindustrial air-sea CO_2 flux patterns based on ocean interior carbon measurements and models. *Geophysical Research Letters*, *30*(1), 1010. https://doi.org/10.1029/2002GL015594

Greenop, R., Hain, M. P., Sosdian, S. M., Oliver, K. I. C., Goodwin, P., Chalk, T. B., et al. (2017). A record of Neogene seawater $\delta^{11}B$ reconstructed from paired $\delta^{11}B$ analyses on benthic and planktic foraminifera. *Climate of the Past*, *13*(2), 149–170. https://doi.org/10.5194/cp-13-149-2017

Groeneveld, J. (2005). Effect of the Pliocene closure of the Panamanian Gateway on Caribbean and east Pacific sea surface temperatures and salinities by applying combined Mg/Ca and, 1–165 pp. Christian Albrechts University, 20 October.

Hansen, J., Lacis, A., Rind, D., Russell, G., Stone, P., Fung, I. Y., et al. (1984). Climate sensitivity: Analysis of feedback mechanisms. In E. Hansen & T. Takahashi (Eds.), *Climate processes and climate sensitivity* (Vol. 29, pp. 130–163). Washington DC: American Geophysical Union. https://doi.org/10.1029/GM029

Hansen, J., Sato, M., Ruedy, R., Nazarenko, L., Lacis, A., Schmidt, G. A., et al. (2005). Efficacy of climate forcings. *Journal of Geophysical Research*, *110*, D18104. https://doi.org/10.1029/2005JD005776

Haug, G. H., Sigman, D. M., Tiedemann, R., Pedersen, T. F., & Sarnthein, M. (1999). Onset of permanent stratification in the subarctic Pacific Ocean. *Nature*, *401*(6755), 779–782. https://doi.org/10.1038/44550

Hays, J., Imbrie, J., & Shackleton, N. J. (1976). Variations in the Earth's orbit: Pacemaker of the ice ages. *Science*, *194*(4270), 1121–1132. https://doi.org/10.1126/science.194.4270.1121

Hemming, N. G., & Hanson, G. N. (1992). Boron isotopic composition and concentration in modern marine carbonates. *Geochimica et Cosmochimica Acta*, *56*(1), 537–543. https://doi.org/10.1016/0016-7037(92)90151-8

Henehan, M. J., Rae, J. W. B., Foster, G. L., Erez, J., Prentice, K. C., Kucera, M., et al. (2013). Calibration of the boron isotope proxy in the planktonic foraminifera *Globigerinoides ruber* for use in palaeo-CO_2 reconstruction. *Earth and Planetary Science Letters*, *364*, 111–122. https://doi.org/10.1016/j.epsl.2012.12.029

Herbert, T. D., Peterson, L. C., Kucera, M. T., & Liu, Z. (2010). Tropical ocean temperatures over the past 3.5 million years. *Science*, *328*, 1530–1534. https://doi.org/10.1126/science.1185435

Higgins, J. A., Kurbatov, A. V., Spaulding, N. E., Brook, E. J., Introne, D. S., Chimiak, L. M., et al. (2015). Atmospheric composition 1 million years ago from blue ice in the Allan Hills, Antarctica. *PNAS*, *112*(22), 6887–6891. https://doi.org/10.1073/pnas.1420232112

Hodell, D. A., & Venz-Curtis, K. A. (2006). Late Neogene history of deepwater ventilation in the Southern Ocean. *Geochemistry, Geophysics, Geosystems*, *7*, Q09001. https://doi.org/10.1029/2005GC001211

Hönisch, B., Allen, K. A., Lea, D. W., Spero, H. J., Eggins, S. M., Arbuszewski, J. A., et al. (2013). The influence of salinity on Mg/Ca in planktic foraminifers—Evidence from cultures, core-top sediments and complementary $\delta^{18}O$. *Geochimica et Cosmochimica Acta*, *121*(C), 196–213. https://doi.org/10.1016/j.gca.2013.07.028

Hönisch, B., & Hemming, N. G. (2004). Ground-truthing the boron isotope-paleo-pH proxy in planktonic foraminifera shells: Partial dissolution and shell size effects. *Paleoceanography*, *19*, PA4010. https://doi.org/10.1029/2004PA001026

Hönisch, B., & Hemming, N. G. (2005). Surface ocean pH response to variations in pCO_2 through two full glacial cycles. *Earth and Planetary Science Letters*, *236*(1–2), 305–314. https://doi.org/10.1016/j.epsl.2005.04.027

Hönisch, B., Hemming, N. G., Archer, D., Siddall, M., & McManus, J. F. (2009). Atmospheric carbon dioxide concentration across the mid-Pleistocene transition. *Science*, *324*(5934), 1551–1554. https://doi.org/10.1126/science.1171477

Horita, J., Zimmermann, H., & Holland, H. D. (2002). Chemical evolution of seawater during the Phanerozoic: Implications from the record of marine evaporites. *Geochimica et Cosmochimica Acta*, *66*(21), 3733–3756. https://doi.org/10.1016/S0016-7037(01)00884-5

Huybers, P. (2007). Glacial variability over the last two million years: An extended depth-derived agemodel, continuous obliquity pacing, and the Pleistocene progression. *Quaternary Science Reviews*, *26*(1–2), 37–55. https://doi.org/10.1016/j.quascirev.2006.07.013

Imbrie, J., Boyle, E. A., Clemens, S. C., Duffy, A., Howard, W. R., Kukla, G., et al. (1992). On the structure and origin of major glaciation cycles 1. Linear responses to Milankovitch forcing. *Paleoceanography*, *7*(6), 701–738. https://doi.org/10.1029/92pa02253

Imbrie, J., Hays, J. D., Martinson, D. G., McIntyre, A., Mix, A. C., Morley, J., et al. (1984). The orbital theory of Pleistocene climate: Support from a revised chronology of the marine $\delta^{18}O$ record. In A. L. Berger, J. Imbrie, J. Hays, G. Kukla, & B. Saltzman (Eds.), *Milankovitch and climate* (pp. 269–305). Dordrecht, Holland: Milankovitch and Climate.

Ishikawa, T., & Nakamura, E. (1993). Boron isotope systematics of marine-sediments. *Earth and Planetary Science Letters*, *117*(3–4), 567–580. https://doi.org/10.1016/0012-821X(93)90103-G

Joannin, S., Cornée, J. J., Münch, P., Fornari, M., Vasiliev, I., Krijgsman, W., et al. (2010). Early Pleistocene climate cycles in continental deposits of the Lesser Caucasus of Armenia inferred from palynology, magnetostratigraphy, and $^{40}Ar/^{39}Ar$ dating. *Earth and Planetary Science Letters*, *291*(1–4), 149–158. https://doi.org/10.1016/j.epsl.2010.01.007

Jouzel, J., Masson-Delmotte, V., Cattani, O., Dreyfus, G., Falourd, S., Hoffmann, G., et al. (2007). Orbital and millennial Antarctic climate variability over the past 800,000 years. *Science*, *317*(5839), 793–796. https://doi.org/10.1126/science.1141038

Key, R. M., Kozyr, A., Sabine, C. L., Lee, K., Wanninkhof, R., Bullister, J. L., et al. (2004). A global ocean carbon climatology: Results from Global Data Analysis Project (GLODAP). *GBC*, *18*(4), 1–23. https://doi.org/10.1029/2004GB002247

Klochko, K., Kaufman, A. J., Yao, W., Byrne, R. H., & Tossell, J. A. (2006). Experimental measurement of boron isotope fractionation in seawater. *Earth and Planetary Science Letters*, *248*(1–2), 276–285. https://doi.org/10.1016/j.epsl.2006.05.034

Köhler, P., & Bintanja, R. (2008). The carbon cycle during the mid Pleistocene transition: The Southern Ocean decoupling hypothesis. *Climate of the Past*, *4*(4), 311–332. https://doi.org/10.5194/cp-4-311-2008

Köhler, P., Bintanja, R., Fischer, H., Joos, F., Knutti, R., Lohmann, G., & Masson-Delmotte, V. (2010). What caused Earth's temperature variations during the last 800,000 years? Data-based evidence on radiative forcing and constraints on climate sensitivity. *Quaternary Science Reviews*, *29*(1–2), 129–145. https://doi.org/10.1016/j.quascirev.2009.09.026

Köhler, P., de Boer, B., von der Heydt, A. S., Stap, L. B., & van de Wal, R. S. W. (2015). On the state dependency of the equilibrium climate sensitivity during the last 5 million years. *Climate of the Past*, *11*(12), 1801–1823. https://doi.org/10.5194/cp-11-1801-2015

Kürschner, W. M., van der Burgh, J., Visscher, H., & Dilcher, D. L. (1996). Oak leaves as biosensors of late Neogene and early Pleistocene paleoatmospheric CO_2 concentrations. *Marine Micropaleontology*, *27*(1–4), 299–312. https://doi.org/10.1016/0377-8398(95)00067-4

Laskar, J., Robutel, P., Joutel, F., Gastineau, M., Correia, A. C. M., & Levrard, B. (2004). A long-term numerical solution for the insolation quantities of the Earth. *Astronomy and Astrophysics*, *428*(1), 261–285. https://doi.org/10.1051/0004-6361:20041335

Lawrence, K., Herbert, T. D., Brown, C. M., Raymo, M. E., & Haywood, A. M. (2009). High-amplitude variations in North Atlantic sea surface temperature during the early Pliocene warm period. *Paleoceanography*, *24*, PA2218. https://doi.org/10.1029/2008PA001669

Lea, D. W. (2004). The 100 000-yr cycle in tropical SST, greenhouse forcing, and climate sensitivity. *Journal of Climate*, *17*(11), 2170–2179. https://doi.org/10.1175/1520-0442(2004)017<2170:TYCITS>

Lee, K., Kim, T.-W., Byrne, R. H., Millero, F. J., Feely, R. A., & Liu, Y.-M. (2010). The universal ratio of boron to chlorinity for the North Pacific and North Atlantic oceans. *Geochimica et Cosmochimica Acta*, *74*(6), 1801–1811. https://doi.org/10.1016/j.gca.2009.12.027

Legrande, A. N., & Schmidt, G. A. (2006). Global gridded data set of the oxygen isotopic composition in seawater. *Geophysical Research Letters*, *33*, L12604. https://doi.org/10.1029/2006GL026011

Lemarchand, D., Gaillardet, J., Lewin, E., & Allegre, C. J. (2000). The influence of rivers on marine boron isotopes and implications for reconstructing past ocean pH. *Nature*, *408*(6815), 951–954. https://doi.org/10.1038/35050058

Lisiecki, L. E. (2010). A benthic $\delta^{13}C$-based proxy for atmospheric pCO_2 over the last 1.5 Myr. *Geophysical Research Letters*, *37*, L21708. https://doi.org/10.1029/2010GL045109

Lisiecki, L. E., & Raymo, M. E. (2005). A Pliocene-Pleistocene stack of 57 globally distributed benthic $\delta^{18}O$ records. *Paleoceanography*, *20*, PA1003. https://doi.org/10.1029/2004PA001071

Locarnini, R. A., Mishonov, A. V., Antonov, J. I., Boyer, T. P., Garcia, H. E., Baranova, O. K., et al. (2013). World ocean atlas 2013, Vol. 1: Temperature. In S. Levitus & A. Mishonov (Eds.), *NOAA Atlas NESDIS 73* (pp. 1–21). Silver Spring, MD: National Oceanic and Atmospheric Administration (NOAA).

Lueker, T. J., Dickson, A. G., & Keeling, C. D. (2000). Ocean pCO_2 calculated from dissolved inorganic carbon, alkalinity, and equations for K_1 and K_2: Validation based on laboratory measurements of CO_2 in gas and seawater at equilibrium. *Marine Chemistry*, *70*(1–3), 105–119. https://doi.org/10.1016/S0304-4203(00)00022-0

Lunt, D. J., Foster, G. L., Haywood, A. M., & Stone, E. J. (2008). Late Pliocene Greenland glaciation controlled by a decline in atmospheric CO_2 levels. *Nature*, *454*(7208), 1102–1105. https://doi.org/10.1038/nature07223

Lüthi, D., le Floch, M., Bereiter, B., Blunier, T., Barnola, J. M., Siegenthaler, U., et al. (2008). High-resolution carbon dioxide concentration record 650,000–800,000 years before present. *Nature*, *453*(7193), 379–382. https://doi.org/10.1038/nature06949

Manabe, S., & Broccoli, A. J. (1985). The influence of continental ice sheets on the climate of an ice-age. *Journal of Geophysical Research*, *90*(ND1), 2167–2190. https://doi.org/10.1029/JD090iD01p02167

Martin, P. A., & Lea, D. W. (2002). A simple evaluation of cleaning procedures on fossil benthic foraminiferal Mg/Ca. *Geochemistry, Geophysics, Geosystems*, *3*(10), 8401. https://doi.org/10.1029/2001GC000280

Martínez-Botí, M. A., Foster, G. L., Chalk, T. B., Rohling, E. J., Sexton, P. F., Lunt, D. J., et al. (2015). Plio-Pleistocene climate sensitivity evaluated using high-resolution CO_2 records. *Nature*, *518*(7537), 49–54. https://doi.org/10.1038/nature14145

Martínez-Botí, M. A., Marino, G., Foster, G. L., Ziveri, P., Henehan, M. J., Rae, J. W. B., et al. (2015). Boron isotope evidence for oceanic carbon dioxide leakage during the last deglaciation. *Nature*, *518*(7538), 219–222. https://doi.org/10.1038/nature14155

Martínez-Garcia, A., Rosell-Melé, A., Jaccard, S. L., Geibert, W., Sigman, D. M., & Haug, G. H. (2011). Southern Ocean dust-climate coupling over the past four million years. *Nature*, *476*(7360), 312–315. https://doi.org/10.1038/nature10310

Martínez-Garcia, A., Rosell-Melé, A., McClymont, E. L., Gersonde, R., & Haug, G. H. (2010). Subpolar link to the emergence of the modern Equatorial Pacific cold tongue. *Science*, *328*(5985), 1550–1553. https://doi.org/10.1126/science.1184480

Mashiotta, T., Lea, D. W., & Spero, H. J. (1999). Glacial-interglacial changes in Subantarctic sea surface temperature and δ^{18}O-water using foraminiferal Mg. *Earth and Planetary Science Letters*, *170*(4), 417–432. https://doi.org/10.1016/S0012-821X(99)00116-8

McClymont, E. L., Rosell-Melé, A., Haug, G. H., & Lloyd, J. M. (2008). Expansion of subarctic water masses in the North Atlantic and Pacific oceans and implications for mid-Pleistocene ice sheet growth. *Paleoceanography*, *23*, PA4214. https://doi.org/10.1029/2008PA001622

Medina-Elizalde, M., & Lea, D. W. (2005). The mid-Pleistocene transition in the tropical Pacific. *Science*, *310*(5750), 1009–1012. https://doi.org/10.1126/science.1115933

Medina-Elizalde, M., Lea, D. W., & Fantle, M. S. (2008). Implications of seawater Mg/Ca variability for Plio-Pleistocene tropical climate reconstruction. *Earth and Planetary Science Letters*, *269*(3–4), 585–595. https://doi.org/10.1016/j.epsl.2008.03.014

Millero, F. J. (1995). Thermodynamics of the carbon dioxide system in the oceans. *Geochimica et Cosmochimica Acta*, *59*(4), 661–677. https://doi.org/10.1016/0016-7037(94)00354-o

Myhre, G., Highwood, E. J., Shine, K. P., & Stordal, F. (1998). New estimates of radiative forcing due to well mixed greenhouse gases. *Geophysical Research Letters*, *25*(14), 2715–2718. https://doi.org/10.1029/98GL01908

Ni, Y., Foster, G. L., Bailey, T., Elliott, T., Schmidt, D. N., Pearson, P. N., et al. (2007). A core top assessment of proxies for the ocean carbonate system in surface-dwelling foraminifers. *Paleoceanography*, *22*, PA3212. https://doi.org/10.1029/2006PA001337

O'Brien, C. L., Foster, G. L., Martínez-Botí, M. A., Abell, R., Rae, J. W. B., & Pancost, R. D. (2014). High sea surface temperatures in tropical warm pools during the Pliocene. *Nature Geoscience*, *7*(8), 606–611. https://doi.org/10.1038/ngeo2194

Paillard, D., Labeyrie, L., & Yiou, P. (1996). Macintosh program performs time-series analysis. *Eos, Transactions American Geophysical Union*, *77*(39), 379–379. https://doi.org/10.1029/96EO00259

Pearson, P. N., & Palmer, M. (2000). Atmospheric carbon dioxide concentrations over the past 60 million years. *Nature*, *406*(6797), 695–699. https://doi.org/10.1038/35021000

Pena, L. D., & Goldstein, S. L. (2014). Thermohaline circulation crisis and impacts during the mid-Pleistocene transition. *Science*, *345*, 318–322. https://doi.org/10.1126/science.1249770

Perez, F. F., & Fraga, F. (1987). The pH measurements in seawater on the NBS scale. *Marine Chemistry*, *21*(4), 315–327. https://doi.org/10.1016/0304-4203(87)90054-5

Petit, J.-R., Jouzel, J., Raynaud, D., Barkov, N. I., Barnola, J.-M., Basile, I., Bender, M. L., et al. (1999). Climate and atmospheric history of the past 420,000 years from the Vostok ice core, Antarctica. *Nature*, *399*(6735), 429–436. https://doi.org/10.1038/20859

Pierrot, D. E. L., Wallace, D. W. R., & Lewis, E. (2006). *MS Excel program developed for CO_2 system calculations*. Berkeley, CA: Carbon Dioxide Information Analysis Center.

Raitzsch, M., & Hönisch, B. (2013). Cenozoic boron isotope variations in benthic foraminifers. *Geology*, *41*(5), 591–594. https://doi.org/10.1130/G34031.1

Ravelo, A. C., & Fairbanks, R. G. (1992). Oxygen isotopic composition of multiple species of planktonic foraminifera: Recorders of the modern photic zone temperature gradient. *Paleoceanography*, *7*(6), 815–831. https://doi.org/10.1029/92PA02092

Raymo, M. E. (1994). The initiation of northern hemisphere glaciation. *Annual Review of Earth and Planetary Sciences*, *22*(1), 353–383. https://doi.org/10.1146/annurev.earth.22.1.353

Raymo, M. E., Lisiecki, L. E., & Nisancioglu, K. (2006). Plio-Pleistocene ice volume, Antarctic climate, and the global δ^{18}O record. *Science*, *313*(5786), 492–495. https://doi.org/10.1126/science.1123296

Raymo, M. E., & Nisancioglu, K. H. (2003). The 41 kyr world: Milankovitch's other unsolved mystery. *Paleoceanography*, *18*(1), 1011. https://doi.org/10.1029/2002PA000791

Regenberg, M., Nürnberg, D., Steph, S., Groeneveld, J., Garbe-Schönberg, D., Tiedemann, R., & Dullo, W.-C. (2006). Assessing the effect of dissolution on planktonic foraminiferal Mg/Ca ratios: Evidence from Caribbean core tops. *Geochemistry, Geophysics, Geosystems*, *7*, Q07P15. https://doi.org/10.1029/2005GC001019

Retallack, G. J. (2009). Greenhouse crises of the past 300 million years. *Geological Society of America Bulletin*, *121*(9–10), 1441–1455. https://doi.org/10.1130/B26341.1

Roy, M., Clark, P. U., Raisbeck, G. M., & Yiou, F. (2004). Geochemical constraints on the regolith hypothesis for the middle Pleistocene transition. *Earth and Planetary Science Letters*, *227*(3-4), 281–296. https://doi.org/10.1016/j.epsl.2004.09.001

Ruddiman, W. F., Raymo, M. E., Martinson, D. G., Clement, B. M., & Backman, J. (1989). Pleistocene evolution: Northern hemisphere ice sheets and North Atlantic Ocean. *Paleoceanography*, *4*(4), 353–412. https://doi.org/10.1029/PA004i004p00353

Russon, T., Elliot, M., Sadekov, A. Y., Cabioch, G., Corrège, T., & De Deckker, P. (2010). Inter-hemispheric asymmetry in the early Pleistocene Pacific warm pool. *Geophysical Research Letters*, *37*, L11601. https://doi.org/10.1029/2010GL043191

Sanyal, A., Bijma, J., Spero, H. J., & Lea, D. W. (2001). Empirical relationship between pH and the boron isotopic composition of *Globigerinoides sacculifer*: Implications for the boron isotope paleo-pH proxy. *Paleoceanography*, *16*(5), 515–519. https://doi.org/10.1029/2000pa000547

Schiebel, R., & Hemleben, C. (2005). Modern planktic foraminifera. *Paläontologische Zeitschrift*, *79*(1), 135–148. https://doi.org/10.1007/BF03021758

Schlitzer, R. (2000). Electronic atlas of WOCE hydrographic and tracer data now available. *Eos, Transactions American Geophysical Union*, *81*(5), 45–45. https://doi.org/10.1029/00EO00028

Schlitzer, R. (2017). Ocean Data View, http://www.odv.awi.de, 4 ed.

Schmidt, G. A., Severinghaus, J., Abe-Ouchi, A., Alley, R. B., Broecker, W., Brook, E., Etheridge, D., et al. (2017). Overestimate of committed warming. *Nature*, *547*(7662), E16–E17. https://doi.org/10.1038/nature22803

Seki, O., Foster, G. L., Schmidt, D. N., Mackensen, A., Kawamura, K., & Pancost, R. D. (2010). Alkenone and boron-based Pliocene pCO_2 records. *Earth and Planetary Science Letters*, *292*(1–2), 201–211. https://doi.org/10.1016/j.epsl.2010.01.037

Shackleton, N. J., Berger, A. L., & Peltier, W. (1990). An alternative astronomical calibration of the lower Pleistocene timescale based on ODP Site 677. *Transactions of the Royal Society of Edinburgh Earth Sciences*, *81*, 251–261. https://doi.org/10.1017/s0263593300020782

Shakun, J. D., Clark, P. U., He, F., Marcott, S. A., Mix, A. C., Liu, Z., Otto-Bliesner, B. L., et al. (2012). Global warming preceded by increasing carbon dioxide concentrations during the last deglaciation. *Nature*, *484*(7392), 49–54. https://doi.org/10.1038/nature10915

Shakun, J. D., Raymo, M. E., & Lea, D. W. (2016). An early Pleistocene Mg/Ca-^{18}O record from the Gulf of Mexico: Evaluating ice sheet size and pacing in the 41-kyr world, 1–17. https://doi.org/10.1002/(ISSN)1944-9186

Shinn, R. A., & Barron, E. J. (1989). Climate sensitivity to continental ice-sheet size and configuration. *Journal of Climate*, *2*(12), 1517–1537. https://doi.org/10.1175/1520-0442(1989)002<1517:CSTCIS>2.0.CO;2

Shipboard Scientific Party (1988). Site 668. In W. Ruddiman, M. Sarnthein, J. Baldauf, et al. (Eds.), *Proceedings of the ocean drilling program, initial reports* (Vol. 108, pp. 931–946). College Station, TX: Ocean Drilling Program.

Sigman, D. M., Jaccard, S. L., & Haug, G. H. (2004). Polar ocean stratification in a cold climate. *Nature*, *428*(6978), 59–63. https://doi.org/10.1038/nature02357

Snyder, C. W. (2016). Evolution of global temperature over the past two million years. *Nature*, *538*, 226–228. https://doi.org/10.1038/nature19798

Spero, H. J., Mielke, K. M., Kalve, E. M., Lea, D. W., & Pak, D. K. (2003). Multispecies approach to reconstructing eastern equatorial Pacific thermocline hydrography during the past 360 kyr. *Paleoceanography*, *18*(1), 1022. https://doi.org/10.1029/2002PA000814

Stults, D. Z., Wagner-Cremer, F., & Axsmith, B. J. (2011). Atmospheric paleo-CO_2 estimates based on *Taxodium distichum* (Cupressaceae) fossils from the Miocene and Pliocene of eastern North America. *Palaeogeography Palaeoclimatology Palaeoecology*, *309*(3–4), 327–332. https://doi.org/10.1016/j.palaeo.2011.06.017

Takahashi, T., Sutherland, S. C., Wanninkhof, R., Sweeney, C., Feely, R. A., Chipman, D. W., et al. (2009). Climatological mean and decadal change in surface ocean pCO_2, and net sea–air CO_2 flux over the global oceans. *Deep Sea Research, Part II*, *56*(8–10), 554–577. https://doi.org/10.1016/j.dsr2.2008.12.009

Thunell, R. C., & Honjo, S. (1981). Calcite dissolution and the modification of planktonic foraminiferal assemblages. *Marine Micropaleontology*, *6*(2), 169–182. https://doi.org/10.1016/0377-8398(81)90004-9

Tripati, A. K., Roberts, C. D., Eagle, R. A., & Li, G. (2011). A 20 million year record of planktic foraminiferal B/Ca ratios: Systematics and uncertainties in pCO_2 reconstructions. *Geochimica et Cosmochimica Acta*, *75*(10), 2582–2610. https://doi.org/10.1016/j.gca.2011.01.018

Tyrrell, T., & Zeebe, R. E. (2004). History of carbonate ion concentration over the last 100 million years. *Geochimica et Cosmochimica Acta*, *68*(17), 3521–3530. https://doi.org/10.1016/j.gca.2004.02.018

Tziperman, E., & Gildor, H. (2003). On the mid-Pleistocene transition to 100-kyr glacial cycles and the asymmetry between glaciation and deglaciation times. *Paleoceanography*, *18*(1), 1001. https://doi.org/10.1029/2001pa000627

von der Heydt, A. S., Dijkstra, H. A., van de Wal, R. S. W., Caballero, R., Crucifix, M., Foster, G. L., et al. (2016). Lessons on climate sensitivity from past climate changes. *Current Climate Change Reports*, *2*(4), 148–158. https://doi.org/10.1007/s40641-016-0049-3

Waddell, L. M., Hendy, I. L., Moore, T. C., & Lyle, M. W. (2009). Ventilation of the abyssal Southern Ocean during the late Neogene: A new perspective from the subantarctic Pacific. *Paleoceanography*, *24*, PA3206. https://doi.org/10.1029/2008PA001661

Wang, Y., Momohara, A., Wang, L., Lebreton-Anberrée, J., & Zhou, Z. (2015). Evolutionary history of atmospheric CO_2 during the late Cenozoic from fossilized Metasequoia needles, edited by W. O. Wong. *PLoS One*, *10*(7), 1–15. https://doi.org/10.1371/journal.pone.0130941

Weldeab, S., Schneider, R. R., & Kölling, M. (2006). Comparison of foraminiferal cleaning procedures for Mg/Ca paleothermometry on core material deposited under varying terrigenous-input and bottom water conditions. *Geochemistry, Geophysics, Geosystems*, *7*, Q04P12. https://doi.org/10.1029/2005GC000990

Witze, A. (2015). Super-fast drills hunt for oldest ice. *Nature*, *526*, 618–619. https://doi.org/10.1038/526618a

York, D., Evensen, N. M., Martínez, M. L., & De Basabe Delgado, J. (2004). Unified equations for the slope, intercept, and standard errors of the best straight line. *American Journal of Physics*, *72*(3), 367–375. https://doi.org/10.1119/1.1632486

Zeebe, R. E., & Wolf-Gladrow, D. A. (2001). *CO_2 in seawater: Equilibrium, kinetics, isotopes*. Elsevier.

Zhang, Y. G., Pagani, M., Liu, Z., Bohaty, S. M., & DeConto, R. (2013). A 40-million-year history of atmospheric CO_2. *Philosophical Transactions of the Royal Society A: Mathematical, Physical and Engineering Sciences*, *371*(2001). https://doi.org/10.1098/rsta.2013.0096

Zweng, M. M., Reagan, J. R., Antonov, J. I., Locarnini, R. A., Mishonov, A. V., Boyer, T. P., et al. (2013). World ocean atlas 2013, Vol. 2: Salinity. In S. Levitus, & A. Mishonov (Eds.), *NOAA Atlas NESDIS 73* (pp. 1–20). Silver Spring, MD: World Ocean Atlas 2013.